

The delayed evolution of high-mass white dwarfs:  
the Q branch and double-white-dwarf mergers

SIHAO CHENG (程思浩),<sup>1</sup> JEFFREY D. CUMMINGS,<sup>1</sup> AND BRICE MÉNARD<sup>1,2</sup>

<sup>1</sup>*Department of Physics and Astronomy, The Johns Hopkins University, 3400 N Charles Street, Baltimore, MD 21218, USA*

<sup>2</sup>*Kavli Institute for the Physics and Mathematics of the Universe, University of Tokyo, Kashiwa 277-8583, Japan*

Submitted to ApJ

ABSTRACT

Studying high-mass white dwarfs (WDs) can shed light on the progenitors of Type Ia supernovae. Recently, the unprecedented power of *Gaia* Data Release 2 (DR2) has revealed an enhancement of high-mass WDs on the H–R diagram, called the Q branch. This branch is located at the high-mass end of the crystallization branch identified by Tremblay et al. (2019). However, investigating its properties, we find that the number density and the velocity distribution of WDs on the Q branch cannot be explained by the cooling delay of crystallization alone, suggesting the existence of an extra cooling delay. To explore the properties of this delay, we statistically compare two age indicators – the dynamical age reflected by transverse velocity and the photometric age – for more than one thousand high-mass WDs ( $1.08 - 1.23 M_{\odot}$ ). We show that, in addition to crystallization and merger delays, an 8-Gyr cooling delay is required on the Q branch, which affects about 7% of high-mass WDs. This is a challenge to WD cooling models. <sup>22</sup>Ne settling in some WDs might account for this extra delay. We also show that  $20 \pm 6\%$  of high-mass WDs originate from double-WD mergers, corresponding to a merger rate of  $(2.1 \pm 0.6) \times 10^{-14} M_{\odot}^{-1} \text{yr}^{-1}$  in their mass range. This is a direct observational constraint on the rate of double-WD mergers, which is a promising channel of Type Ia supernova explosion.

*Keywords:* Hertzsprung–Russell and colour–magnitude diagrams — methods: statistical — stars: kinematics and dynamics — supernovae: general — white dwarfs

1. INTRODUCTION

Until recently, explorations of the white dwarf region in the Hertzsprung–Russell (H–R) diagram were severely limited by the number of objects with available distance estimates. The European Space Agency *Gaia* mission (Gaia Collaboration et al. 2016) has changed this situation drastically. *Gaia* is an all-sky survey of astrometry and photometry for stars down to 20.7 magnitude. The H–R diagram of white dwarfs generated by *Gaia* Data Release 2 (DR2) reveals three branch-like features, illustrated as the A, B, and Q branches<sup>1</sup> in figure 13 of Gaia Collaboration et al. (2018b). The A and B branches have been understood as standard-mass white dwarfs

( $m_{\text{WD}} \sim 0.6 M_{\odot}$ ) with hydrogen-rich and helium-rich atmospheres, respectively (e.g., Bergeron et al. 2019). However, the Q branch, as an enhancement of high-mass white dwarfs ( $m_{\text{WD}} > 1.0 M_{\odot}$ ), is still not fully understood. This is a challenge for current white dwarf evolutionary models and an opportunity for studying high-mass white dwarfs.

White dwarfs evolve along their cooling tracks on the H–R diagram. Unlike the A and B branches, the Q branch is not aligned with any cooling track or iso-age curves, suggesting that it is caused by a delay of cooling instead of a peak in mass or age distribution. As the cooling is delayed on the Q branch, white dwarfs pile-up there. The Q branch coincides with the high-mass region of the crystallization branch identified by Tremblay et al. (2019). As a liquid-to-solid phase transition in the white dwarf core, crystallization releases energy through latent heat (e.g., van Horn 1968) and phase separation (e.g., Garcia-Berro et al. 1988; Segretain et al. 1994; Is-

s.cheng@jhu.edu

<sup>1</sup> Named after the presence of DA, DB, and DQ white dwarfs (Gaia Collaboration et al. 2018a), respectively. These are spectral types of white dwarfs. DA white dwarfs have hydrogen lines in their spectra. DB and DQ are for helium and carbon lines

ern et al. 1997), which can indeed create a cooling delay. However, the observed pile-up on the Q branch is higher and narrower than expected from standard crystallization models (Tremblay et al. 2019, figure 4), suggesting that an extra cooling delay may exist in addition to crystallization.

Another possible delay in the evolution of high-mass white dwarfs comes from binary evolution, and it offers an opportunity to better understand double-white-dwarf (double-WD) mergers. Double-WD merger is a promising channel of producing Type Ia supernovae (i.e. the double-degenerate channel, see e.g., Webbink 1984; Iben & Tutukov 1984; Tutukov et al. 1992; Maoz et al. 2010; Mennekens et al. 2010; Maoz et al. 2014; Sato et al. 2015; Liu et al. 2018; Shen et al. 2018a,b), and simulations of binary evolution show that double-WD merger products may also account for a considerable fraction of high-mass white dwarfs (e.g., Ruiter et al. 2009; Toonen et al. 2012; Yungelson & Kuranov 2017, Temmink et al., in prep.). However, in observation, this fraction and the double-WD merger rate are still a matter of debate (e.g., Giammichele et al. 2012; Rebassa-Mansergas et al. 2015; Tremblay et al. 2016; Maoz et al. 2018). Using the age–velocity–dispersion relation of stars in the milky-way disc, Wegg & Phinney (2012) translate the merger delay into velocity excess and use the velocity distribution of high-mass white dwarfs to constrain the fraction of merger products. Unfortunately, they did not get a strong constraint because of the small sample size. But now, thanks to the large and homogeneous sample in *Gaia* DR2, one can get a much better constraint following the same idea. The analysis will also be more comprehensive with both the extra cooling delay and the merger delay taken into account.

In addition, the core composition of double-WD merger products is different from high-mass white dwarfs formed from single-star evolution. The former have carbon+oxygen (C/O) cores whereas the latter are believed to hold oxygen+neon (O/Ne) cores. It is natural to search for the signature of this composition difference in white dwarf cooling behavior. We will show that the extra cooling delay may apply only to C/O-core white dwarfs, and thus the Q branch may also be an observational evidence for double-WD mergers.

The layout of this paper is as follows: in section 2 we describe our white dwarf sample; in sections 3 we show the existence of the extra cooling delay on the Q branch; in section 4 we build a Bayesian model treating both the two delays in high-mass white dwarf evolution; in sections 5 we use velocity distribution to constrain the properties of the extra delay and the fraction of merger products; in section 6 we discuss the origin of the extra

delay and the DQ white dwarfs on the Q branch, and we calculate the double-WD merger rate; we conclude our results in section 7.

## 2. DATA

We use data from *Gaia* DR2 (Gaia Collaboration et al. 2018b), which for the first time provides parallaxes  $\varpi$  and proper motions  $\mu$  that are derived purely from *Gaia* measurements. *Gaia* DR2 also provides Vega magnitudes of each object in three wide pass-bands:  $G$ ,  $G_{BP}$ , and  $G_{RP}$ . The  $G$  band spans from 350 to 1000 nm, and the  $G_{BP}$  and  $G_{RP}$  bands are mainly the blue and red parts of the  $G$  band, separated at the  $H\alpha$  transition (Gaia Collaboration et al. 2016).

### 2.1. Sample selection

Gentile Fusillo et al. (2019) have compiled a catalog of *Gaia* DR2 white dwarfs based on  $G$  band absolute magnitude, *Gaia* colour index, and some quality cuts. To select only white dwarfs with high-precision measurements, we further apply the following cuts:

$$\sigma_{G_{BP}-G_{RP}} < 0.10, \quad (1)$$

$$\sigma_{\mu}/\varpi < 2 \text{ km s}^{-1}, \quad (2)$$

$$\text{parallax\_over\_error} > 8, \quad (3)$$

$$\text{astrometric\_excess\_noise} < 1.5, \quad (4)$$

$$\text{phot\_bp\_rp\_excess\_factor} < 1.4, \quad (5)$$

$$1000 / \text{parallax} < 250, \quad (6)$$

where the colour error  $\sigma_{G_{BP}-G_{RP}}$  is defined as the root mean square of the photometric errors in  $G_{BP}$  and  $G_{RP}$  bands, the proper motion error  $\sigma_{\mu}$  as the the root mean square of the two components of proper motion errors, and  $\varpi$  parallax. These cuts are designed to balance data quality and sample size, and we do not attempt to get a volume-complete sample. Nevertheless, these cuts do not introduce kinematic biases.

### 2.2. Quantity definitions

Our analysis requires white dwarf absolute magnitude, colour index, and the two components of transverse velocity  $\mathbf{v}_T = (v_L, v_B)$ . Except the colour index  $G_{BP} - G_{RP}$ , which is directly read from `bp_rp`, we derive the other quantities in the following way:

$$M_G = G - 5 \log(\varpi/\text{mas}^{-1}) - 10, \quad (7)$$

$$v_L = \frac{\mu_L - (A \cos 2l + B) \cos b}{\varpi}, \quad (8)$$

$$v_B = \frac{\mu_B + A \sin 2l \sin b \cos b}{\varpi}, \quad (9)$$

where  $G$  and  $\varpi/\text{mas}^{-1}$  are read from *Gaia* DR2 columns `phot_g_mean_mag` and `parallax`,  $\mu_L$  and  $\mu_B$  are converted from columns `ra`, `dec`, `pmra`, and `pmdec` with the

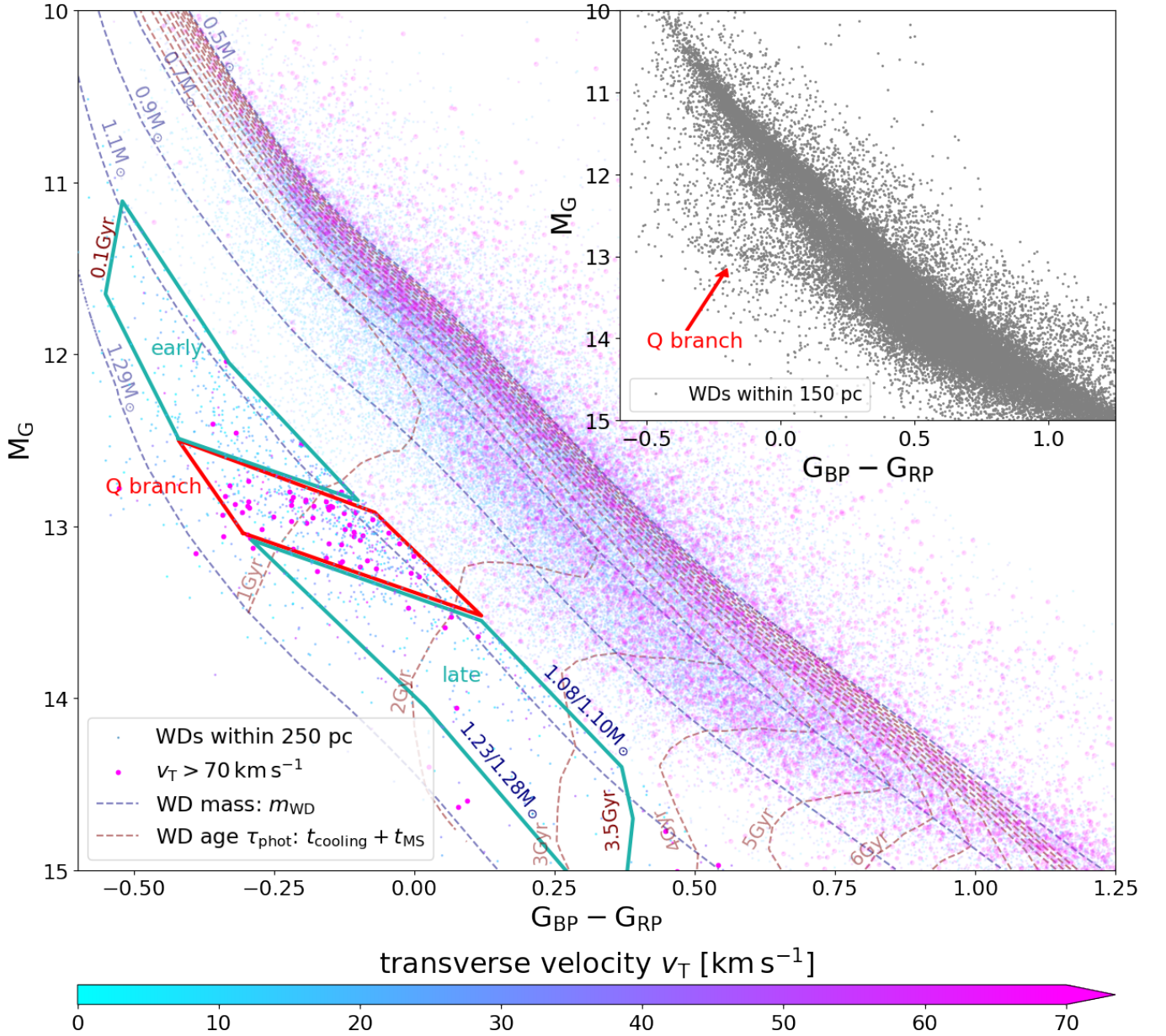


**Figure 1.** The H–R diagram of WDs with high-precision astrometric and photometric measurements. In the top-right panel we show the distribution of WDs (for visualisation purpose we use an 150-pc sample). The Q branch is the over-density marked by the red arrow. In the main panel, we colour-code WDs within 250 pc with their transverse velocities with respect to the local standard of rest. Fast WDs ( $v_T > 70 \text{ km s}^{-1}$ ) are emphasized by large symbols, and high-mass WDs ( $> 1.08 M_\odot$ ) are emphasized by high symbol opacity. The grid of WD masses and total ages is also plotted (using the O/Ne model for high-mass WDs). The Q branch divides the cooling tracks of high-mass WDs into three segments: the ‘early’, ‘Q branch’, and ‘late’ segments, each with different signatures of the extra cooling delay. We also mark the mass range of these segments with dark blue texts: the first mass is derived from the O/Ne-core WD model and the second is from the C/O-core WD model. According to the age–velocity-dispersion relation (AVR), fast WDs are old. However, a bulk of fast WDs is concentrated on the Q branch, with photometric ages only 1 – 2 Gyr, indicating a long delay during their evolution. The merger delay is only about 2 Gyr and does not focus on the branch, so there must be an extra delay of WD cooling on the branch.

coordinate conversion function in the `ASTROPY` package (Astropy Collaboration et al. 2013, 2018),  $A$  and  $B$  are the Oort constants taken from Bovy (2017). We do not correct for extinction because at within the distance cut extinction is in general tiny and there is no accurate estimate for it. To avoid the influence of hyper-velocity white dwarfs, we further impose a velocity cut:

$$v_T = \sqrt{v_L^2 + v_B^2} < 200 \text{ km s}^{-1}, \quad (10)$$

which also excludes many halo white dwarfs. We point out that *Gaia* does not provide any useful radial velocity information for white dwarfs as they have no spectral lines in the 845 – 872 nm wavelength range of *Gaia*'s spectrometer (Gaia Collaboration et al. 2016).

We then derive white dwarf photometric ages  $\tau_{\text{phot}}$  and masses  $m_{\text{WD}}$  from the H–R diagram coordinates ( $G_{\text{BP}} - G_{\text{RP}}, M_G$ ), based on single-star evolution scenario and white dwarf cooling models. The main-sequence ages are estimated with the initial–final mass relation from Cummings et al. (2018) and a simple age–mass relation  $t_{\text{MS}} = (m_{\text{MS}}/M_{\odot})^{-3} \times 10 \text{ Gyr}$ . For high-mass white dwarfs, the main-sequence ages are negligible. The white dwarf cooling models include a catalog of synthetic colours calibrated to nearby white dwarfs (Holberg & Bergeron 2006; Kowalski & Saumon 2006; Tremblay et al. 2011; Bergeron et al. 2011) and a grid of white dwarf cooling tracks (Fontaine et al. 2001). We use the synthetic colour catalog for thick-hydrogen atmosphere ( $m_{\text{H}}/m_{\text{WD}} = 10^{-4}$ ) and the cooling tracks for C/O-core white dwarfs<sup>2</sup>. In order to convert any H–R diagram positions into  $m_{\text{WD}}$  and  $\tau_{\text{phot}}$ , we linearly interpolate these models between grid points. Stellar models show that in the single-star-evolution scenario white dwarfs heavier than about 1.05 – 1.10  $M_{\odot}$  have oxygen+neon (O/Ne) cores (e.g., Siess 2007; Lauffer et al. 2018). So, we combine the cooling tracks of  $m_{\text{WD}} \leq 1.05 M_{\odot}$  C/O white dwarfs with the four cooling tracks of  $m_{\text{WD}} \geq 1.10 M_{\odot}$  O/Ne white dwarfs (Camisassa et al. 2019).

The O/Ne white dwarf model only gives slightly lower mass estimate than the C/O white dwarf model (e.g., 1.08 – 1.23  $M_{\odot}$  in the O/Ne and C/O WD combined model corresponds to 1.10 – 1.28  $M_{\odot}$  in the C/O WD model), and their estimates of the photometric ages are similar for the white dwarfs we are interested in ( $\tau_{\text{phot}} < 3.5 \text{ Gyr}$ ); switching between thick-hydrogen, thin-hydrogen, and helium atmosphere models does not influence the photometric age estimates much, either.

<sup>2</sup> <http://www.astro.umontreal.ca/~bergeron/CoolingModels/>. The synthetic colours for the revised Gaia DR2 pass-bands are not yet available on this website and were kindly provided by P. Bergeron via private communication.

We remind the readers that the photometric ages  $\tau_{\text{phot}}$  derived from single-star evolution plus white dwarf cooling models may not be the true ages  $\tau$ . Their difference comes from the aforementioned extra cooling delay and merger delay.

### 3. A QUALITATIVE EXAMINATION OF THE Q BRANCH

In Figure 1, we show the white dwarfs selected in section 2.1. In the top-right panel, we show the distribution of white dwarfs on the H–R diagram. The Q branch is a factor-two enhancement at around  $-0.4 < G_{\text{BP}} - G_{\text{RP}} < 0.2$  and  $M_G = 13$ . In the main panel, we colour-code white dwarfs within 250 pc by their transverse velocities  $v_T$  with respect to the local standard of rest. We adopt the values  $(U_{\odot}, V_{\odot}, W_{\odot}) = (11, 12, 7) \text{ km s}^{-1}$  from Schönrich et al. (2010) to correct for the solar reflex motion. We emphasize the fast white dwarfs ( $v_T > 70 \text{ km s}^{-1}$ ) in Figure 1 with bigger dots: they are very likely thick-disc stars. We also plot the grid of white dwarf masses  $m_{\text{WD}}$  and photometric ages  $\tau_{\text{phot}}$  derived from the combined O/Ne-core and C/O-core white dwarf cooling model. The cooling tracks are the curves with constant  $m_{\text{WD}}$ . White dwarfs with different birth times form a ‘white dwarf cooling flow’ on the H–R diagram as they move along their cooling tracks.

We focus on the mass range where the Q branch is most prominent. To maximize sample size and minimize the contamination from standard-mass helium-atmosphere white dwarfs (the B branch), we impose a photometric age and mass cut for further analysis:

$$0.1 \text{ Gyr} < \tau_{\text{phot}} < 3.5 \text{ Gyr}, \quad (11)$$

$$1.08 M_{\odot} < m_{\text{WD}} < 1.23 M_{\odot}, \quad (12)$$

where  $m_{\text{WD}}$  is derived from the combined cooling model for O/Ne-core and C/O-core white dwarfs. This corresponds to 1.10 – 1.28  $M_{\odot}$  in the C/O-core-only cooling model. In this region, the Q branch divides the white dwarf cooling flow into three segments: the early, Q branch, and late segments, as shown in Figure 1. We define the Q-branch segment by

$$|M_G - 1.2 \times \text{bp\_rp} - 13.2| < 0.2 \quad (13)$$

in addition to the previous age and mass cuts. The early and late segments are then defined as the regions earlier and later than the Q-branch segment along the cooling tracks, respectively.

Below, we show evidence of the extra cooling delay and explain the importance of using velocity information in addition to number-density enhancement. We then show that this delay is at least a few billion years long and



affects only a small fraction of high-mass white dwarfs. Merger delay will be treated later in our quantitative model.

### 3.1. An extra cooling delay is needed

As argued by Tremblay et al. (2019), an enhancement not aligned with mass or age grid, such as the Q branch, should be produced by a slowing down of white dwarf cooling. This kind of cooling delay creates a ‘traffic jam’ in the white dwarf flow, and the Q branch (and the crystallization branch) is a snapshot of this traffic jam. *Is crystallization alone enough to explain the cooling delay on the Q branch?* If it does, the distribution of photometric ages  $\tau_{\text{phot}}$  calculated from a model including crystallization effects, should no longer carry any signature of the Q branch. However, observations lead to the antithesis. In the upper panel of Figure 2 we show the distribution of  $\tau_{\text{phot}}$  in three mass ranges. We use a 150-pc sample here because larger sample suffers severely from incompleteness. The signature of Q-branch enhancement is still clear. Therefore, an extra cooling delay in addition to crystallization effects (latent heat and phase separation) must exist.

In general, not all white dwarfs need to have this extra delay. So, we use two parameters – the fraction  $f_{\text{extra}}$  of influenced high-mass white dwarfs and the delay time  $t_{\text{extra}}$  – to describe this extra cooling delay. In the lower panel of Figure 2 we show a sketch of this generic two-population scenario. Before the Q branch, the ‘extra-delayed population’ has no difference from the normal population; on the branch, the extra-delayed population cools slower, which causes to effects: its number density is enhanced, and the age discrepancies (i.e. the delay) between the true ages and  $\tau_{\text{phot}}$  also build up; after the branch, the number-density enhancement disappears, but the age discrepancy remains.

The observed extra enhancement  $A_{\text{obs}}$  can be expressed as (with constant formation rates for both populations assumed):

$$A_{\text{obs}} \equiv \frac{n_{\text{on branch}}}{n_{\text{off branch}}} - 1 = f_{\text{extra}} A = \frac{f_{\text{extra}} t_{\text{extra}}}{\Delta t_{\text{branch}}}, \quad (14)$$

where  $n$  is the number density per photometric-age interval,  $A$  is the intrinsic enhancement of the extra-delayed population itself,  $\Delta t_{\text{branch}}$  is the width of the Q-branch segment in terms of photometric age, for which we adopt an average value  $\Delta t_{\text{branch}} = 0.74$  Gyr. There is clearly a degeneracy between  $f_{\text{extra}}$  and  $t_{\text{extra}}$  in this two-population scenario if only one observable  $A_{\text{obs}}$  is measured. To break this degeneracy, we seek for another way to observationally constrain  $f_{\text{extra}}$  and  $t_{\text{extra}}$ .

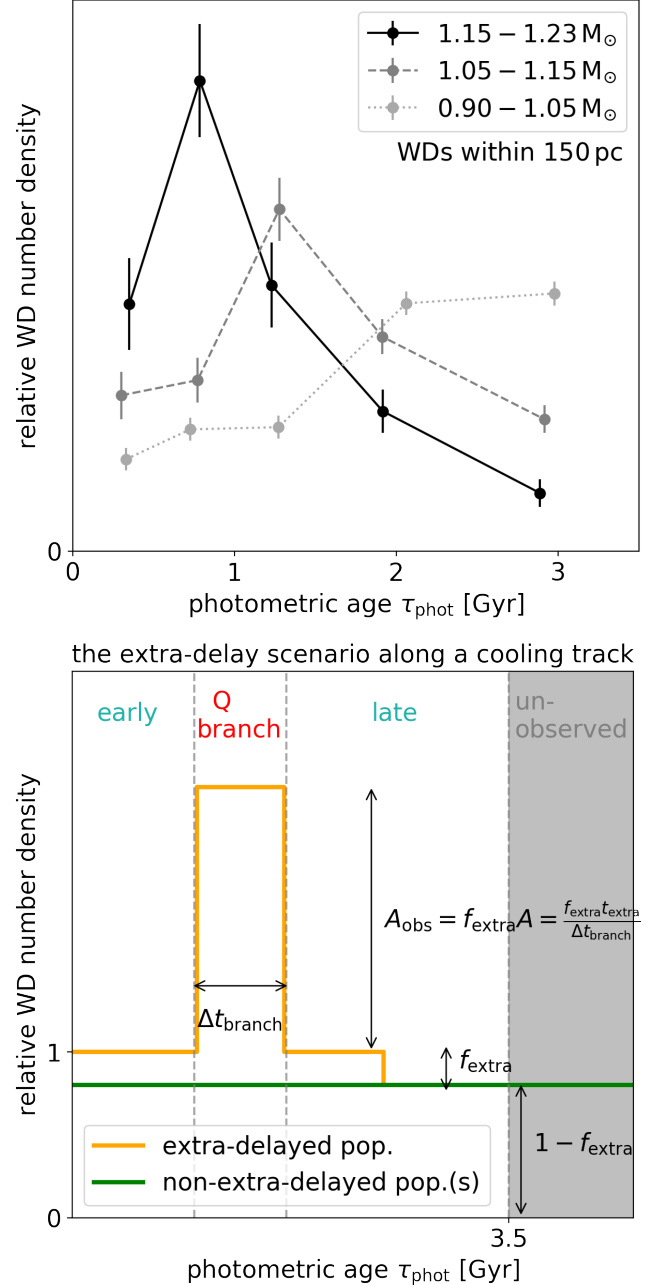


**Figure 2.** *Upper:* The photometric age  $\tau_{\text{phot}}$  distribution (normalised) of high-mass WDs in three mass ranges.  $\tau_{\text{phot}}$  is calculated from a model including crystallization effects. Because the Q-branch enhancement (the peaks whose corresponding ages shift older when WD mass decreases) is still clearly visible for  $m_{\text{WD}} > 1.05 M_{\odot}$ , there must be an extra cooling delay in addition to crystallization. The deficit of old WDs is due to low completeness.

*Lower:* a sketch of the extra-delay scenario. The axes are the same as the upper panel, except the x-axis range is slightly different. In general, there can be some WDs subject to the extra cooling delay and the rest of them not, corresponding to the extra-delayed and non-extra-delayed population in the figure. We also illustrate the quantities of equation 14.

### 3.2. Constraints from velocity information

Observations show that the velocity dispersion of disc stars is related to stellar ages  $\tau$  (e.g., Holmberg et al. 2009). Therefore, the transverse velocities  $v_T$  of white dwarfs derived from *Gaia* DR2 can be used as a ‘dynamical’ indicator of the true age  $\tau$ . For the milky-way thin disc, the transverse velocity dispersion approximately follows a power law increasing from about  $25 \text{ km s}^{-1}$  at 1.5 Gyr to  $55 \text{ km s}^{-1}$  at around 6-8 Gyr (e.g., Holmberg et al. 2009). The following features on Figure 1 also validate the use of transverse velocity as an age indicator: we observe that most of fast white dwarfs (big, magenta dots) are standard-mass white dwarfs, which have long main-sequence ages and are therefore old when they become white dwarfs; we also observe that most high-mass white dwarfs, which should be young, have low transverse velocities around  $20 - 30 \text{ km s}^{-1}$ .

We then use the velocity distribution in the early, Q branch, and late segments to analyze the extra-delay time  $t_{\text{extra}}$  and extra-delayed population fraction  $f_{\text{extra}}$ . In Figure 1 we observe a strong excess of white dwarfs with  $v_T > 70 \text{ km s}^{-1}$  in the Q-branch segment. According to the age–velocity–dispersion relation (AVR) mentioned above, these fast white dwarfs are most likely old thick disc stars. Given the photometric age on the Q branch is only  $0.5 - 2 \text{ Gyr}$ , the extra delay of these white dwarfs must be more than a few billion years. In the upper panel of Figure 3 we show that the excess of fast white dwarfs in the Q-branch segment is observed for a variety of velocity cuts; in the lower panel we show that it is clearest for  $m_{\text{WD}} > 1.05 M_{\odot}$ . Merger delay and stronger effects of crystallization cannot explain Figure 3, because neither of them can make a higher fraction of fast white dwarfs on the ‘Q branch’ than in the ‘late’ segment. The only way to create such a feature in is to have a long extra delay applicable to a small fraction of white dwarfs: a long delay makes enough fast white dwarfs on the branch, and a small fraction guarantees that the extra-delayed population is diluted in the ‘late’ region. Also, this scenario keeps the observed enhancement  $A_{\text{obs}}$  reasonable. To summarise, the qualitative examination of velocity distributions indicates a small population fraction  $f_{\text{extra}}$  and a long extra delay time  $t_{\text{extra}}$  of the extra-delayed population.

## 4. A QUANTITATIVE INFERENCE OF THE TWO EVOLUTIONARY DELAYS

In the previous section, we used qualitative arguments to analyze the extra-delayed population fraction and delay time. However, several limitations prevent us from deriving more robust quantitative estimates: the AVR describes a statistical relation between age and velocity,

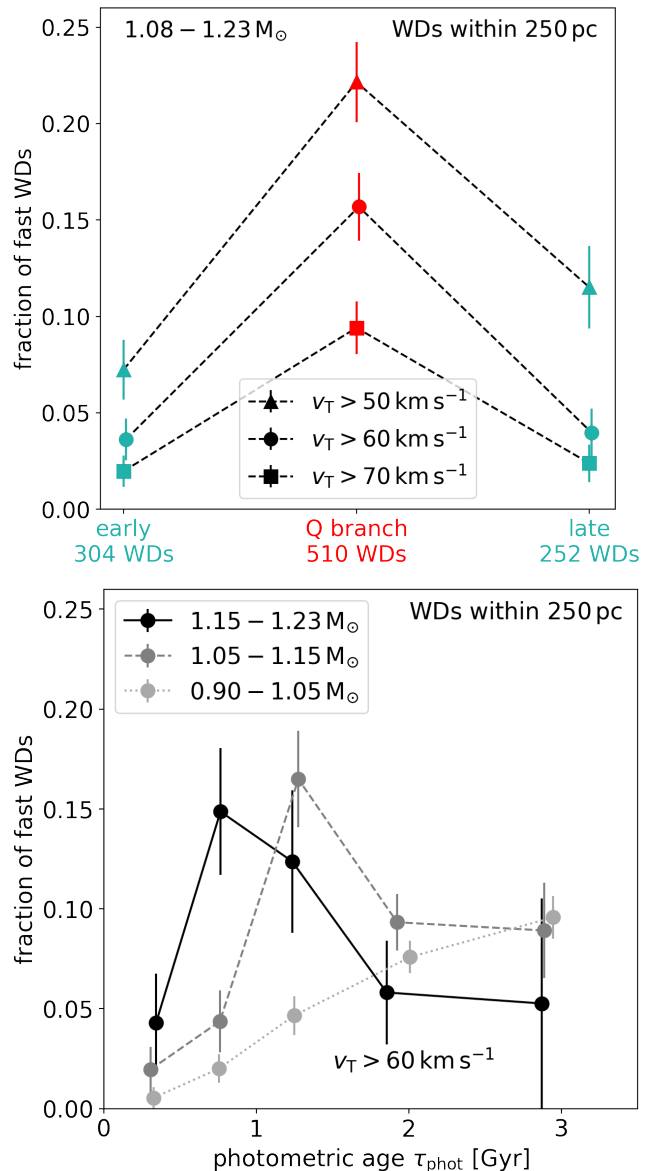


**Figure 3.** The fraction of fast white dwarfs with a variety of velocity cuts (*upper panel*) and in different mass ranges (*lower panel*). This fraction on the Q branch is significantly higher than in the segments both before and after the Q branch, which indicates a small  $f_{\text{extra}}$  and long  $t_{\text{extra}}$  of the extra-delayed population. Since the problem of incompleteness (selection effect) does not bias velocity distribution, we use WDs within 250 pc.

so one cannot get the exact stellar age for an individual white dwarf; the velocity distribution is not isotropic, so the projected transverse velocity distribution depends on white dwarf positions on the sky; in addition, double-WD merger delay should also be taken into account. These difficulties compel us to make a statistical model that includes both delays and describes the velocity distributions of all populations of high-mass white dwarfs.

**Table 1.** Delay scenarios of the three populations. The total delay  $\Delta t = \tau - \tau_{\text{phot}}$  for each population and each segment is also shown.  $\Delta t$ ,  $\Delta t_{\text{merger}}$ , and  $\Delta t_{\text{extra}}$  are not single numbers but follow their distributions. They are used to calculate the true ages  $\tau$  from photometric ages  $\tau_{\text{phot}}$ .

Population (abbreviation)	single-star evolution (s)	extra-delayed (extra)	double-WD merger (non-extra-delayed) (m)
merger delay	no	yes or no (setup 1 or 2)	yes
extra cooling delay	no	yes	no
early	0	$\Delta t_{\text{merger}}$ or 0	$\Delta t_{\text{merger}}$
Q branch	0	$(\Delta t_{\text{extra}} + \Delta t_{\text{merger}})$ or $\Delta t_{\text{extra}}$	$\Delta t_{\text{merger}}$
late	0	$(t_{\text{extra}} + \Delta t_{\text{merger}})$ or $t_{\text{extra}}$	$\Delta t_{\text{merger}}$

By doing so, we may also make use of the full constraining power of the observations instead of collapsing information into a few arbitrary bins.

#### 4.1. Description of the model

To model the distribution of white dwarfs, we consider the following white dwarf populations: a generic population that evolves singly and follows standard cooling model, a double-WD merger population with systematic age offsets (i.e., the merger delay), and the extra-delayed population with the extra cooling delay on the Q branch. To make our model robust to outliers such as halo white dwarfs, extreme kick-outs, and systematic errors of our model, we also include a background population. Accordingly, the overall distribution  $p$  of observables can be written as a weighted average of the distributions  $p_x$  for each population  $x$ :

$$p = f_s p_s + f_m p_m + f_{\text{extra}} p_{\text{extra}} + f_{\text{bg}} p_{\text{bg}}, \quad (15)$$

where ‘s’ represents the generic single-star evolution, ‘m’ merger, ‘extra’ the extra-delayed, and ‘bg’ the background population; the weight  $f_x$  denotes the fraction of each population, satisfying  $f_s + f_m + f_{\text{extra}} + f_{\text{bg}} = 1$ .

Our goal is to use observations to constrain the three independent population fractions ( $f_m$ ,  $f_{\text{extra}}$ , and  $f_{\text{bg}}$ ) and the length of extra cooling delay  $t_{\text{extra}}$ , which is encoded in the distribution  $p_{\text{extra}}$ . We have two sets of observables: transverse velocities  $\mathbf{v}_T$  and photometric ages  $\tau_{\text{phot}}$ . They are connected by the AVR  $p(\mathbf{v}|\tau)$  and the delay scenario of each population. The delay

$$\Delta t = \tau - \tau_{\text{phot}} \quad (16)$$

includes the contribution from the extra and/or the merger delays, for which we list the properties in Table 1. These two delays can be statistically distinguished, because they have different influences in the three cooling segments. Moreover, we explore two extreme situations as our model setups, which are also listed in Table 1:

- setup 1: *all* white dwarfs of the extra-delayed population also have merger delay;
- setup 2: *no* white dwarfs of the extra-delayed population has merger delay;

Our model is similar to that of Wegg & Phinney (2012), but it includes the extra-delayed population and uses 1066 high-mass white dwarfs, much larger than the sample Wegg & Phinney (2012) use. In addition, to avoid the need for modelling selection effects, we derive our constraints only from velocity information. The free parameters of our model include the 3 population fractions, the extra delay time  $t_{\text{extra}}$ , and parameters for AVR and solar motion. Although constraints on the AVR and solar motion already exist, treating them also as free parameters can avoid potential systematic errors, and the comparison of our best-fitting values with the existing values allows us to check the validity of our method. Since the model parameters are constrained by more than 2000 observations (two velocity components for each white dwarf), it is not problematic to increase the number of parameters from a few to a dozen.

The main assumptions and simplifications in our model are as follows. (i) We assume that upon entering the ‘Q branch’ segment, all members of the extra-delayed population suddenly slow down their cooling by a constant factor, and upon leaving the branch, the cooling rates suddenly resume, so that we may parametrize this delay by just its length  $t_{\text{extra}}$  and population fraction  $f_{\text{extra}}$ . (ii) The velocity distribution of white dwarfs is a superposition of 3-D Gaussian distributions as a function of age  $\tau$  only, i.e.  $p(\mathbf{v}|\tau) = \mathcal{N}(\mathbf{v}_0(\tau), \Sigma(\tau))$ . (iii) The true age distribution of high-mass white dwarfs within 250 pc is uniform up to 11 Gyr, i.e.  $\tau \sim U[0, 11 \text{ Gyr}]$ . (iv) Moreover, we do not model the errors of observables because they are in general small and very costly to model.

#### 4.2. Bayesian framework

We follow a Bayesian approach to build our model. This means that we can first build a forward model outputting the likelihood probability density function (PDF) of observables  $\mathbf{y}$  given model parameters  $\boldsymbol{\theta}$ :

$$\mathcal{L} \equiv p(\mathbf{y}|\boldsymbol{\theta}), \quad (17)$$

and then obtain the posterior PDF of model parameters  $p(\boldsymbol{\theta}|\mathbf{y})$  from the observed value of  $\mathbf{y}$  through the Bayesian Theorem:

$$p(\boldsymbol{\theta}|\mathbf{y}) \propto \mathcal{L} \cdot p(\boldsymbol{\theta}), \quad (18)$$

where  $p(\boldsymbol{\theta})$  is the prior PDF of the parameters. Finally, we use the Markov-Chain Monte-Carlo (MCMC) method to sample the posterior distribution and estimate the parameters of interest after marginalising nuisance parameters. In the three steps, the key part is to construct the likelihood.

As each white dwarf provides an independent observation, the likelihood  $\mathcal{L}$  in our model can be written as the product of the likelihoods of each individual white dwarf:

$$\mathcal{L} = \prod_i p_i(\mathbf{y}_i|\boldsymbol{\theta}). \quad (19)$$

To avoid a direct dependence on selection effects, we use conditional likelihood to let the constraining power originate only from velocity distributions: we define the individual likelihood  $p_i$  as the probability density for the  $i^{\text{th}}$  white dwarf to have transverse velocity  $\mathbf{v}_T$  given all other observables of this white dwarf:

$$p_i \equiv p(\mathbf{v}_T | \{\tau_{\text{phot}}, m_{\text{WD}}, l, b\}_i, \boldsymbol{\theta}). \quad (20)$$

We condition on  $\tau_{\text{phot}}$  and  $m_{\text{WD}}$  because their distributions are influenced by the detection completeness, quality cuts, and white dwarf spatial distribution. Besides, the mass  $m_{\text{WD}}$  in equation 20 model is only used to identify whether a white dwarf is on the Q branch. In order to decompose the three populations, we derive:

$$\begin{aligned} p(\mathbf{v}_T | \tau_{\text{phot}}, m_{\text{WD}}) &= \frac{p(\mathbf{v}_T, \tau_{\text{phot}}, m_{\text{WD}})}{p(\tau_{\text{phot}}, m_{\text{WD}})} \\ &= \frac{\sum_x f_x p_x(\mathbf{v}_T, \tau_{\text{phot}}, m_{\text{WD}})}{\sum_x f_x p_x(\tau_{\text{phot}}, m_{\text{WD}})}, \end{aligned} \quad (21)$$

where the sums are taken over  $x$  with possible values ‘s’, ‘m’, ‘extra’, and ‘bg’ representing different populations. To make use of the known distributions such as the AVR, we employ the probability identity:

$$\begin{aligned} p(\mathbf{v}_T, \tau_{\text{phot}}) &= \int p(\mathbf{v}_T | \tau_{\text{phot}}, \tau) p(\tau_{\text{phot}}, \tau) d\tau \\ &= \int p(\mathbf{v}_T | \tau) p(\tau_{\text{phot}}, \tau) d\tau \end{aligned} \quad (22)$$

(where the second step is valid because velocity is only a function of the true age  $\tau$ ) and another identity:

$$p(\tau_{\text{phot}}) = \int p(\tau_{\text{phot}}, \tau) d\tau. \quad (23)$$

We also assume the age distribution is uniform,  $\tau \sim U[0, 11 \text{ Gyr}]$ . In this way, the likelihood PDF in equation 19 and 20 can be expressed through the delay distributions  $p(\Delta t)$  and a velocity model  $p(\mathbf{v}_T|\tau)$ .

#### 4.3. Delay distributions

The three white dwarf populations in our model are defined by their different delay signatures  $\Delta t$ , which may comprise two evolutionary delays: the extra cooling delay  $\Delta t_{\text{extra}}$  and merger delay  $\Delta t_{\text{merger}}$ . The latter is the amount of time before a double-WD binary merges and restarts its cooling process<sup>3</sup>. It produces a systematic age offset but does not change the cooling rate. The delay scenario of each population in each segment is listed in Table 1.

The extra cooling delay  $\Delta t_{\text{extra}}$  is created in the Q-branch segment. So, we assume that on the branch it follows a uniform distribution,  $\Delta t_{\text{extra}} \sim U[0, t_{\text{extra}}]$ . We remind the readers that  $\Delta t_{\text{extra}}$  is a random variable with probability distribution, whereas  $t_{\text{extra}}$  is the upper limit of  $\Delta t_{\text{extra}}$ , a model parameter to be constrained. In theory, the distribution of  $t_{\text{extra}}$  is related to the position on the H–R diagram, because the white dwarfs at the younger part of the Q-branch segment have just started to slow down their cooling and accumulated less cooling delay, but those at the older part are about to leave the Q branch and have accumulated longer cooling delay. Nevertheless, we do not use this piece of information in practice, because the white dwarf atmosphere differences and parallax errors make it hard to determine accurately if a white dwarf has just started or is about to finish their extra cooling delay based on its position on the H–R diagram. Therefore, a uniform distribution is a good and efficient approximation for the extra cooling delay  $\Delta t_{\text{extra}}$ .

For the distribution of double-WD merger delay  $\Delta t_{\text{merger}}$ , we refer to binary population synthesis results (Toonen et al. 2012, 2014, and private communication) and approximate it by

$$p(\Delta t_{\text{merger}}) \propto \Delta t_{\text{merger}}^{-0.7} \quad (24)$$

for merger delay  $\Delta t_{\text{merger}}$  larger than 0.5 Gyr and zero for shorter delay time.

<sup>3</sup> We only consider the double-WD mergers because other mergers such as MS-RG, MS-MS, and MS-WD mergers usually only create  $< 0.2 \text{ Gyr}$  delay, and therefore indistinguishable from the generic population in terms of delay.



## 4.4. Velocity model

In this section, we model the relation between white dwarf transverse velocities  $\mathbf{v}_T$  and their true stellar ages  $\tau$  using the age-velocity-dispersion relation (AVR). The velocity distribution of disc stars in the solar neighbourhood with respect to the local standard of rest can be approximated as 3-D Gaussian distributions (e.g., Binney & Tremaine 2008):

$$p(\mathbf{v}|\tau) = \frac{\exp[-\frac{1}{2}(\mathbf{v} - \mathbf{v}_0)^T \boldsymbol{\Sigma}^{-1}(\mathbf{v} - \mathbf{v}_0)]}{\sqrt{8\pi^3 |\boldsymbol{\Sigma}|}}, \quad (25)$$

whose mean and covariance matrix are determined by stellar age  $\tau$ . We define the  $U$ ,  $V$ ,  $W$  axes as pointing towards  $(l = 0^\circ, b = 0^\circ)$ ,  $(l = 90^\circ, b = 0^\circ)$ , and  $(b = 90^\circ)$ , respectively. The mean velocity  $\mathbf{v}_0(\tau)$  is determined by two effects: the solar reflex motion  $(-U_\odot, -V_\odot, -W_\odot)$  with respect to the local standard of rest and the asymmetric drift in  $V$  direction by  $-\sigma_U^2/80 \text{ km s}^{-1}$  (e.g., Binney & Tremaine 2008). We set the solar motion as free parameters and use them to check the validity of our model.

In section 2 we derived the two components of transverse velocity  $\mathbf{v}_T = (v_L, v_B)^T$ . To model the distribution of this quantity, we project the 3-D Gaussian distribution  $p(\mathbf{v}|\tau)$  onto the tangential plane for each white dwarf and marginalise the radial component  $v_R$ . Thus, we get the PDF of transverse velocities  $p(\mathbf{v}_T|\tau, l, b)$ , which is a 2-D Gaussian distribution for a given age:

$$p(\mathbf{v}_T|\tau, l, b) = \frac{\exp[-\frac{1}{2}(\mathbf{v}_T - \mathbf{v}_{T0})^T \boldsymbol{\Sigma}_{LB}^{-1}(\mathbf{v}_T - \mathbf{v}_{T0})]}{\sqrt{4\pi^2 |\boldsymbol{\Sigma}_{LB}|}}, \quad (26)$$

where the covariance matrix  $\boldsymbol{\Sigma}_{LB}(\tau, l, b)$  and mean  $\mathbf{v}_{T0}(\tau, l, b)$  are calculated from  $\boldsymbol{\Sigma}(\tau)$ ,  $\mathbf{v}_0(\tau)$ , and  $(l, b)$ . Detailed rotation transformation and projection are presented in Appendix A. We use the condition on  $(l, b)$  to avoid modelling the spatial selection effects and reduce unnecessary parameters and biases.

Then, we parametrize the AVR to explicitly express the covariance matrix  $\boldsymbol{\Sigma}(\tau)$  in equation 25. We assume that the main axes of the Gaussian distribution is approximately aligned with  $X$ ,  $Y$ ,  $Z$  directions, so  $\boldsymbol{\Sigma}(\tau)$  can be expressed as a diagonal matrix with elements  $\sigma_U^2(\tau)$ ,  $\sigma_V^2(\tau)$ , and  $\sigma_W^2(\tau)$  in the  $XYZ$  coordinate system. Observations show that the AVR in each direction can be fit by a shifted power law. The power index in the disc plane is around 0.35 and that in the  $Z$  direction is around 0.5 (e.g., Holmberg et al. 2009; Sharma et al. 2014). For old stars including thick disc members, the AVR is still a matter of debate (e.g., Yu & Liu 2018; Mackereth et al. 2019). So, in each direction, we

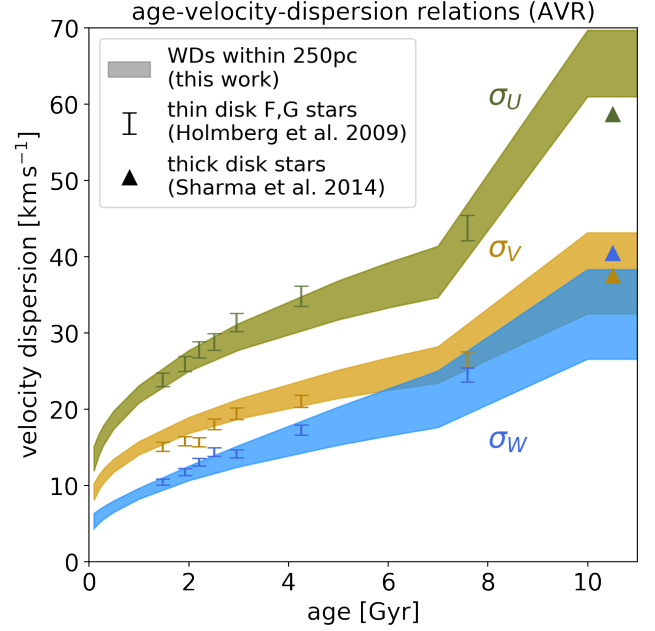


**Figure 4.** The comparison of AVRs from the literature and constrained by this work. The shaded regions show the 16th and 84th percentiles of the AVR posterior constrained by our high-mass WD sample. Symbols with error bars are the AVR measured for main-sequence stars in GCS and RAVE (Holmberg et al. 2009; Sharma et al. 2014). In our model, the  $\tau < 3.5$  Gyr part of AVR is mainly constrained by the non-extra-delayed WDs, and the older part by the extra-delayed WDs. Note that the shape of our AVR for old stars reflects our choice of parametrization.

use a shifted power law to parametrize the AVR of the younger, thin-disc stars:

$$\sigma(\tau) = \sigma^{\tau=0} + \Delta\sigma^{0 \rightarrow 4} \times \left(\frac{\tau}{4}\right)^\beta, \quad \tau < 7 \text{ Gyr}, \quad (27)$$

and we use a constant value  $\sigma^{\text{Thick}}$  to represent the velocity dispersion of stars older than 10 Gyr (thick-disc stars); in between 7 Gyr and 10 Gyr, we linearly interpolate the values from the two ends to reflect the increasing fraction of thick-disc stars. The ratio of the two in-disc components  $\sigma_V$  and  $\sigma_U$  should be a constant for a local sample (e.g., Binney & Tremaine 2008), so we set  $\sigma_V(\tau) = k\sigma_U(\tau)$ . As the assumption of Gaussian distribution gradually breaks down when  $\sigma_U$  increases, we allow the ratio  $k$  to be different for the thin and thick discs. Thus, we use in total 10 parameters to model the AVR: two initial velocity dispersion  $\sigma_{U,W}^{\tau=0}$ , two dispersion increases  $\Delta\sigma_{U,W}^{0 \rightarrow 4}$  between 0 Gyr and 4 Gyr, two power indices  $\beta_{U,W}$ , two thick-disc dispersion  $\sigma_{U,W}^{\text{Thick}}$ , and two in-disc dispersion ratios  $k^{\text{thin}}, k^{\text{Thick}}$ . As mentioned above, the best-fitting values of these parameters can be checked against existing estimates presented in the literature.

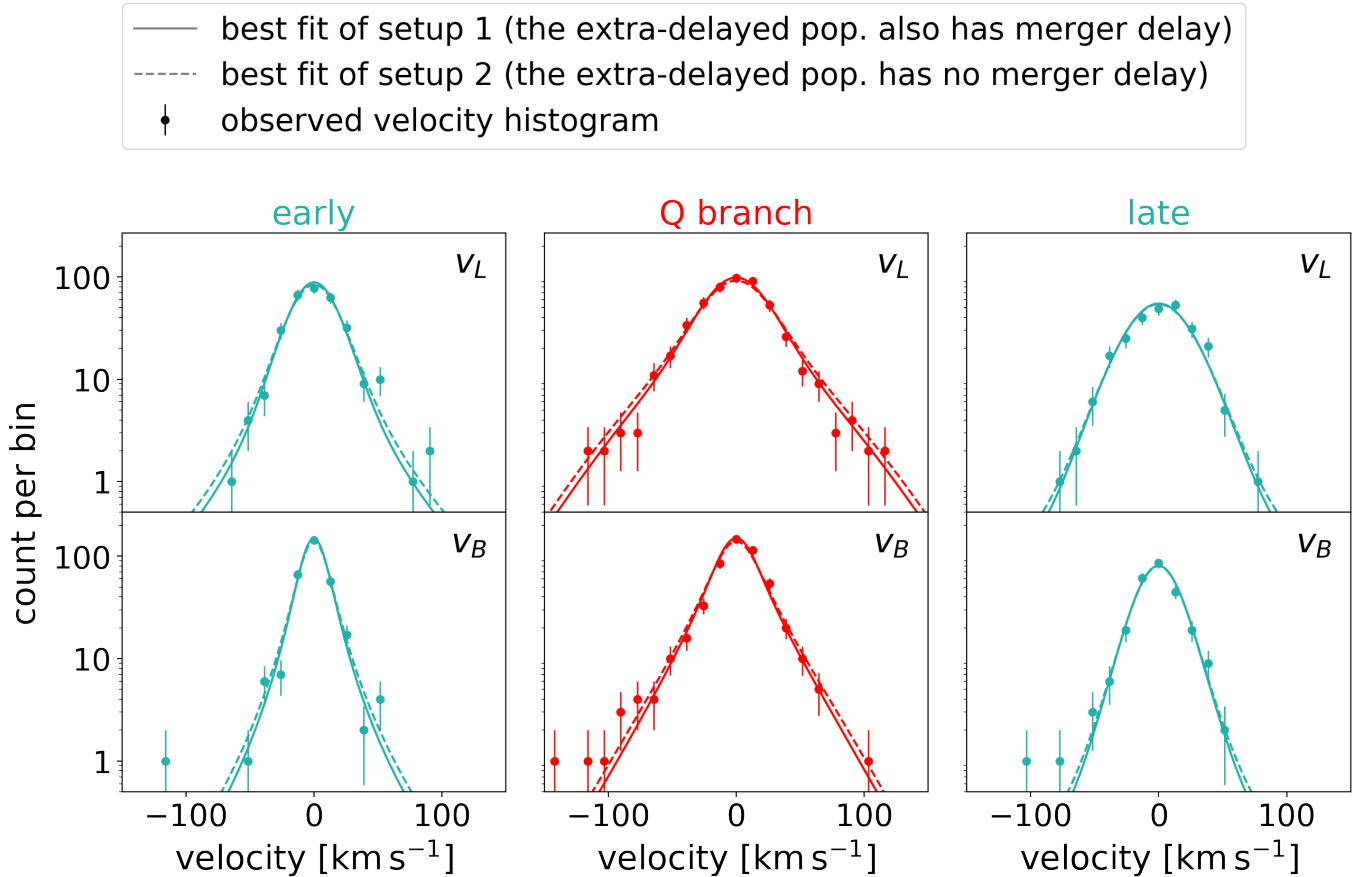


**Figure 5.** The goodness of fitting: a comparison between the observed distributions of transverse velocity and the model predictions under the best-fitting parameters.  $v_L$  and  $v_B$  are the two components of transverse velocity along the galactic longitude and latitude directions. For the observed distribution, we calculate the histogram in the range  $-150 \sim 150 \text{ km s}^{-1}$  with 31 bins, and their error-bars are represented by the square roots of the count in each bin. Note that the y-axis is in logarithmic scale. For the model predictions, we use the properly normalised likelihood function under the best-fitting parameters (see section 5 for details), and it fits well to the observed velocity histograms in all six panels. The solid and dashed curves correspond to the two setups explained in section 4.1 and Table 1, which do not differ much in terms of goodness of fitting. The corresponding best-fitting parameters also produce reasonable AVRs (see Figure 4), which further validates our model.

## 5. RESULTS

To constrain the parameters of our model and obtain estimates for the extra-delay properties and the merger fraction, we feed our Bayesian model with the 1066 white dwarfs in the early, Q branch, and late segments selected in section 2 and 3. We use an MCMC sampler to obtain the posterior distribution of parameters. Details of the MCMC sampler is described in Appendix B.

### 5.1. Validation of the model

First, we present the constraints on solar motion and the AVR and show that they are all in good agreement with estimates from the literature. For the solar motion we obtain the constraint:

$$(U, V, W)_\odot = (10.1 \pm 1.0, 6.7 \pm 1.0, 6.6 \pm 0.5) \text{ km s}^{-1}, \quad (28)$$

which is consistent with Rowell & Kilic (2019)’s measurement using kinematics of mainly standard-mass white dwarfs. Our values of  $U_\odot$  and  $W_\odot$  are also consistent with the results of Schönrich et al. (2010). The discrepancy of  $V_\odot$  measurement is a complicated problem and beyond the scope of this paper.

Our constraint of white dwarf AVR is presented in Figure 4, which shows good consistency with the AVR of both thin- and thick-disc main-sequence stars (Holmberg et al. 2009; Sharma et al. 2014). Removing either the extra-delayed population or merger population leads to unreasonably higher AVRs. Before *Gaia* DR2 came out, Anguiano et al. (2017) noticed an unexpectedly high AVR for young white dwarfs (their figure 21 and 22) and suggested additional heating of the milky-way disc. Now, it is clear that this anomaly is not from additional disc heating but due to not including the extra cool-

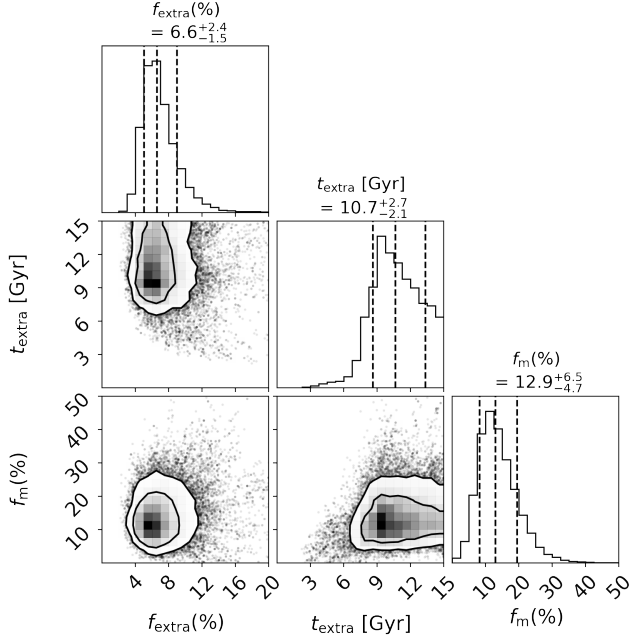


**Figure 6.** The posterior distribution of main parameters of our model.  $f_{\text{extra}}$  is the fraction of the extra-delayed population,  $t_{\text{extra}}$  is the length of the extra cooling delay on the Q branch,  $f_m$  is the fraction of other double-WD merger products. These fractions are proportional to the production rate of each population. These constraints are under setup 1, i.e. assuming all members of the extra-delayed population have merger delays. In this case,  $f_{\text{extra}} + f_m$  rather than  $f_m$  is the total fraction of merger products.

ing delay and merger delay in the age estimate. This unreasonably-high AVR is exactly what we see when we remove the extra-delayed and/or merger population from our model. Therefore, we verify that both the extra cooling delay and the merger delay are necessary.

The background fraction  $f_{\text{bg}}$ , which is designed to capture the small amount of halo stars and absorb the residuals between the model and observations, is found to be  $0.5 \pm 0.4\%$ , which is also consistent with the fraction of halo stars in the solar neighbourhood (given that we have cut out some of the halo components by the data selection of equation 10). The results are similar for setup 1 and setup 2.

The above three checks allow us to validate the use of 14 parameters in the model. The remaining parameters are  $t_{\text{extra}}$ ,  $f_{\text{extra}}$ , and  $f_m$ . Before examining their best-fitting values, we can check the goodness of fitting to verify that the best-fitting model can reproduce the observed velocity distributions. For a meaningful comparison, we again use a conditional likelihood PDF  $p(v_{L/B}|\{l, b, \tau_{\text{phot}}, m_{\text{WD}}\}_i, \theta)$  to eliminate the incompleteness. We calculate this transverse velocity like-

lihood for each white dwarf with the ‘best-fitting’ model (using the median values of each parameter posterior distribution from the MCMC as the model parameters) and then average these likelihoods. Figure 5 shows the observed and predicted velocity distributions in the early, Q branch, and late segments, respectively. As can be seen, our best-fitting models (in both setups 1 and 2) provide good characterisations of the observed velocity distribution in all three segments.

## 5.2. Constraints on the main parameters

Having demonstrated that (i) our model leads to the solar kinematics and age–velocity–dispersion relation (AVR) in agreement with estimates from the literature, (ii) it shows the necessity for two different types of delays, and (iii) it provides a good fit to the observed velocity distributions in each segments of the cooling tracks, we can now examine the constraints we obtain for the main parameters of interest:  $t_{\text{extra}}$ ,  $f_{\text{extra}}$ ,  $f_m$ . In Figure 6, we show the constraints for these three parameters for setup 1. We find that the extra-delayed population fraction is

$$f_{\text{extra}} = 6.6^{+2.4}_{-1.5}\% \text{ or } 9.8^{+5.3}_{-3.0}\%, \text{ (setup 1 or 2),} \quad (29)$$

and the length of the extra delay on the Q branch is

$$t_{\text{extra}} \geq 8 \text{ Gyr or } \geq 10 \text{ Gyr.} \quad (30)$$

This confirms our qualitative conclusion that  $f_{\text{extra}}$  is low and  $t_{\text{extra}}$  is long (see section 3.2). We point out that the difference between these two setups is exactly where the peak of the merger-delay distribution is located (2 Gyr); also, we point out that this lower limit for  $t_{\text{extra}}$  depends on the parametrization of AVR: if we reduce the youngest thick-disc age in our AVR from 7 to 6 Gyr and make the thin-to-thick-disc transition quicker (which is possible according to Mackereth et al. 2019), this lower limit will also decrease by about 1–2 Gyr, but it is hard to further reduce it. The fraction of mergers *without* the extra delay is found to be  $f_m = 13^{+7}_{-5}\%$  or  $18^{+6}_{-5}\%$ . Therefore, the total fraction of double-WD mergers among high-mass white dwarfs is

$$f_{\text{extra}} + f_m = 20^{+7}_{-5}\% \text{ or } f_m = 19^{+6}_{-5}\% \quad (31)$$

among  $1.08 - 1.23 M_{\odot}$  white dwarfs. This total double-WD merger fraction is mainly constrained by the fast white dwarfs in the early segment (where the two setups do not differ from each other), so the constraints on this fraction under setups 1 and 2 are similar. This fraction is also amazingly close to the results of binary population synthesis obtained by Temmink et al. 2019 (in prep). Finally, we calculate the contribution of extra-delayed

population in the Q-branch segment according to the above fractions:

$$F_{\text{extra}} = \frac{f_{\text{extra}}(t_{\text{extra}}/\Delta t_{\text{branch}} + 1)}{1 + f_{\text{extra}}t_{\text{extra}}/\Delta t_{\text{branch}}} \simeq (48 \pm 9)\%, \quad (32)$$

which will be useful in later analysis.

To summarise, we have been able to constrain  $f_{\text{extra}}$ ,  $t_{\text{extra}}$  and  $f_{\text{m}}$ . To do so, we have used the model of evolutionary delays and kinematics described in section 4. Our model uses 17 parameters but 13 of those are standard solar and Galactic kinematic parameters for which we find values consistent with those existing in the literature. By using only information originating from velocities, our constraints are not directly sensitive to selection effects affecting the spatial distribution of the white dwarf sample. Finally, we point out that the constraints on the fraction of double-WD mergers for setup 1 and 2 are similar, i.e. it does not depend on whether or not the extra-delayed white dwarfs are also merger products.

## 6. DISCUSSION

### 6.1. *The energy source of the extra delay: $^{22}\text{Ne}$ settling in merger products?*

Our model has allowed us to use *Gaia* data to constrain the properties of the extra cooling delay on the Q branch. With these phenomenological properties, we can now attempt to understand the physical mechanism responsible for it. In this section, we argue that the  $^{22}\text{Ne}$  settling in previously-metal-rich double-WD merger products may explain the extra delay on the Q branch.

To produce the extra delay revealed by the velocity analysis, an extra energy source is needed, and it should satisfy the following requirements:

1. it has a peaked effect around crystallization;
2. it applies only to a fraction  $f_{\text{extra}} \sim 7\%$  of high-mass white dwarfs;
3. it is powerful enough to create an extra delay  $t_{\text{extra}}$  of at least 8 Gyr (in addition to crystallization delay and merger delay).

Available energy sources are limited. The latent heat and phase separation during crystallization are already included in the cooling model we use. Moreover, they apply to all white dwarfs. So, they cannot explain the extra delay. Another possible energy source is the redistribution of minor elements in white dwarfs. Among all impurities,  $^{22}\text{Ne}$  has the most significant influence on white dwarf cooling (Isern et al. 1991; Bildsten & Hall

2001), because it can be very abundant in a white dwarf, and it feels a net downward force in the white dwarf core. Below, we explore if the redistribution of  $^{22}\text{Ne}$  satisfies all the above requirements.

$^{22}\text{Ne}$  is produced from the C, N, and O in the progenitor stars of white dwarfs. In the hydrogen burning stage, the CNO cycle builds up the slowest reactant  $^{14}\text{N}$ ; then, in the helium burning stage,  $^{14}\text{N}$  is converted into  $^{22}\text{Ne}$ . This leads to an abundance  $X_{^{22}\text{Ne}}^{\text{WD}} \approx Z_{\text{CNO}}^{\text{star}} \approx 0.02$  for solar-metallicity stars (Isern et al. 1991). Due to the additional two neutrons,  $^{22}\text{Ne}$  nuclei feel more downward force of gravity than the upward force from pressure gradient (Bildsten & Hall 2001). Therefore,  $^{22}\text{Ne}$  settles down to the white dwarf centre, and releases gravitational energy.

The amount of energy released by  $^{22}\text{Ne}$  settling (also called  $^{22}\text{Ne}$  sedimentation or  $^{22}\text{Ne}$  diffusion in the literature) depends on the white dwarf mass, composition, and its progenitor metallicity (Deloye & Bildsten 2002; García-Berro et al. 2008; Althaus et al. 2010; Camisassa et al. 2016). García-Berro et al. (2008) modelled the effect of  $^{22}\text{Ne}$  settling for  $1.06 M_{\odot}$ ,  $Z = 0.02$ , C-core and O-core white dwarfs, finding a 0.2 – 3 Gyr additional cooling delay for different setups of the diffusion coefficient ( $D$  value) of  $^{22}\text{Ne}$  and core composition; Althaus et al. (2010) calculated for  $1.0 M_{\odot}$ ,  $Z = 0.03$  and  $Z = 0.06$ , C/O-core white dwarfs and found a 2.6 Gyr and a 4.1 Gyr additional delay with a conservative  $D$  value ( $D = D_s$ ). So, the additional delay time depends on the core composition, progenitor metallicity, diffusion coefficient, and white dwarf mass.

We first show that the  $^{22}\text{Ne}$  settling effect peaks around crystallization (the first requirement). In Figure 7 we present the cooling rate reciprocal  $\zeta^{-1}$  along a cooling track in García-Berro et al. (2008)’s cooling models (their figure 13) of pure-C and pure-O white dwarfs and Fontaine et al. (2001)’s model of a  $1.05 M_{\odot}$  C/O-core white dwarf. For the model with the strongest  $^{22}\text{Ne}$  settling (the yellow, dashed curve), a peaked slowing-down, and therefore number density enhancement, is indeed created around crystallization.

The key to understanding why the energy release from  $^{22}\text{Ne}$  can produce such a peaked effect around crystallization is as follows. Firstly, the number density enhancement  $A$  is determined by the ratio of the extra energy to the white dwarf luminosity rather than the extra energy itself:

$$A = \frac{\zeta^{-1}}{\zeta_0^{-1}} - 1 = \frac{1}{L_{\text{surf}}/L_{\text{extra}} - 1}, \quad (33)$$

where  $\zeta$  and  $\zeta_0$  are the cooling rates with and without the extra energy,  $L_{\text{surf}} \propto T_{\text{eff}}^4$  is the white dwarf lu-



minosity, and  $L_{\text{extra}}$  is the power of the extra energy release. Before crystallization, the power of  $^{22}\text{Ne}$  settling  $L_{\text{extra}}^{\text{Ne}}$  is nearly constant (see Appendix C). So, the constant  $L_{\text{extra}}$  will create a sharply increasing enhancement when  $L_{\text{surf}}$  drops quickly with  $T_{\text{eff}}$  and approaches  $L_{\text{extra}}^{\text{Ne}}$ . Secondly, as the settling cannot happen in solid phase,  $L_{\text{extra}}^{\text{Ne}}$  will be suppressed after crystallization. Thus, as the white dwarf cools down,  $L_{\text{extra}}^{\text{Ne}}$ 's increasing fractional contribution to  $L_{\text{surf}}$  and its final suppression together may create a peak of enhancement around crystallization.

$^{22}\text{Ne}$  settling also satisfies the second requirement for the extra-delay energy source, i.e. it applies only to a fraction of white dwarfs. For a given mass, only the white dwarfs with significant  $^{22}\text{Ne}$  settling (high  $L_{\text{extra}}^{\text{Ne}}$ ) will have the extra cooling delay.  $L_{\text{extra}}^{\text{Ne}}$  is determined by the progenitor metallicity and core composition: the highest  $L_{\text{Ne}}$  is produced in high-mass C/O white dwarfs with metal-rich progenitors (equation C7). As a white dwarf from single-star evolution cannot both harbour a C/O-core and be heavier than about  $1.08 M_{\odot}$  (e.g., Siess 2007), such white dwarfs with maximum  $^{22}\text{Ne}$  settling effect can only be found among double-WD mergers.

There are two possible problems of the  $^{22}\text{Ne}$  explanation: (1) no cooling model has shown that it can create an extra delay as long as 8 Gyr, which is the third requirement for the extra energy source; and (2) there is a slight offset between the observed Q branch and the predicted peak of enhancement (Figure 7). However, the existing cooling models have not explored the mass range above  $1.06 M_{\odot}$ , where the Q branch is most clearly seen. In addition, there are still uncertainties in the cooling model (such as the  $^{22}\text{Ne}$  diffusion coefficient), and the offset can be partly explained by the existence of He-rich-atmosphere white dwarfs. Therefore, neither of the two problems can yet rule out  $^{22}\text{Ne}$  settling as the origin of the extra delay.

### 6.2. Wide-binary fractions on the Q branch

In the previous section we proposed a connection between the extra-delayed population and double-WD binaries. One way to test this idea is to check the wide-binary fractions of white dwarfs on and off the Q branch. If the extra-delayed population indeed comes from double-WD mergers, the kick velocity of a few  $\text{kms}^{-1}$  (e.g., Dan et al. 2014) during the merger may destroy many wide-separation binary systems. To test this idea against observations, we cross-match the wide binaries in *Gaia* DR2 (El-Badry & Rix 2018, 2019) with our high-mass white dwarfs sample. In the early, Q branch, and late segments respectively, we find 5, 4, 7 white dwarfs with main-sequence or white dwarf com-

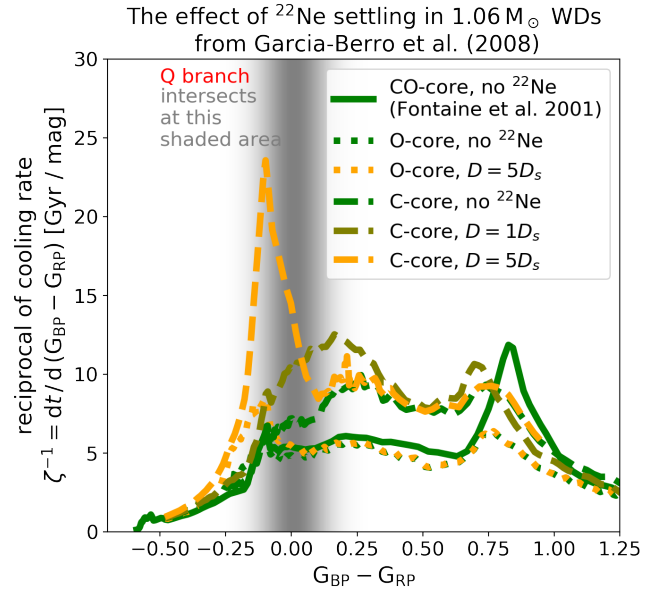


**Figure 7.** A comparison of the influence of  $^{22}\text{Ne}$  settling. The x-axis is the colour index along the cooling track, reflecting white dwarf surface temperatures. The y-axis is the inverse of cooling rate, proportional to the H-R diagram number density. The white dwarf mass ( $1.06 M_{\odot}$ ) of these models is smaller than our sample. Line styles indicate different core compositions and colours indicate the settling speed. The model with the largest settling speed ( $D = 5D_s$  and C-core, see equation C7) produces the highest number density enhancement. Note that the x-axis is different from that of Figure 2, so the green curve is not flat.

panions out of 304, 510, 252 white dwarfs. So, the wide-binary fraction *on* the Q branch is  $0.8 \pm 0.4\%$  compared to the value  $2.2 \pm 0.5\%$  *off* the branch. Although this is just a  $2\sigma$  difference due to small-number statistics, it is still notable. If we assume that the extra-delayed population does not contribute any wide-separation binary system, the wide-binary fraction of non-extra-delayed populations *on* the Q branch becomes  $4/[510 \times (1 - F_{\text{extra}})] = (1.5 \pm 0.8)\%$ , consistent with the *off* branch value  $2.2 \pm 0.5\%$  within  $1\sigma$ . Therefore, the fraction of wide-binaries provides additional support to the idea that the extra-delayed population originates from double-WD mergers.

### 6.3. DQ white dwarfs on the Q branch

Based on spectra features, white dwarfs can be classified as DA-type (with only hydrogen lines; most white dwarfs are of DA-type), DB-type (with only helium lines), DQ-type (with carbon lines), DC-type (no lines), etc. The Q branch is named after the presence of DQ-type white dwarfs on it, which is abnormal and likely to belong to only the extra-delayed population. To get the information of the spectroscopically-verified white

**Table 2.** The statistics of velocity and spectral type of white dwarfs on the Q branch. The fraction of fast DQs are consistent of its belonging purely to the extra-delayed population.

250 pc spectro- scopic sample	all	DQ	DA
all $v_T$	76	19	53
$v_T > 50 \text{ km s}^{-1}$	23	8	14
	$30 \pm 6\%$	$42 \pm 15\%$	$26 \pm 7\%$
$v_T > 60 \text{ km s}^{-1}$	16	7	8
	$21 \pm 5\%$	$37 \pm 14\%$	$15 \pm 6\%$
$v_T > 70 \text{ km s}^{-1}$	9	2	6
	$12 \pm 4\%$	$11 \pm 7\%$	$11 \pm 5\%$

dwarfs, we cross-match our white dwarf sample in *Gaia* DR2 with the Montreal white dwarf database MWDD (Dufour et al. 2017)<sup>4</sup>. Most high-mass DQs are concentrated on the Q branch (Figure 8), and the fraction of fast DQs is very high (Table 2). Combining these two pieces of information, we believe that all these ‘Q-branch DQs’ belong to the extra-delayed population. Then, we estimate that

$$F_{\text{DQ}} = 19/(76F_{\text{extra}}) = (52 \pm 16)\% \quad (34)$$

of extra-delayed white dwarfs are DQ-type white dwarfs. Changing the distance limit of the sample does not influence this result much. We also checked the spatial distribution of these DQs and found no concentration in any direction of the sky.

The DQ white dwarfs on the Q branch are abnormal, because the convection zone in a normal white dwarf with similar temperature is not deep enough to dredge carbon up (Dufour et al. 2005), therefore carbon cannot stay in the atmosphere and sinks down very quickly. In a similar way, the ‘hot DQ’ white dwarfs discovered by Dufour et al. (2007) are also abnormal. In Figure 8, we show the distributions of Q-branch DQs and hot DQs on the H–R diagram. Although Gentile Fusillo et al. (2019) classified the Q-branch DQs also as hot DQs, there are quite a few differences between them.

Hot DQ white dwarfs are characterised by their high surface temperature ( $> 18000 \text{ K}$ ), highly carbon-dominant atmosphere (Williams et al. 2013), high rate of having magnetic field (Dufour et al. 2010, 2013), high rate of being variable and possibly rotating (e.g., Dufour et al. 2009; Dunlap et al. 2010; Dufour et al. 2011;

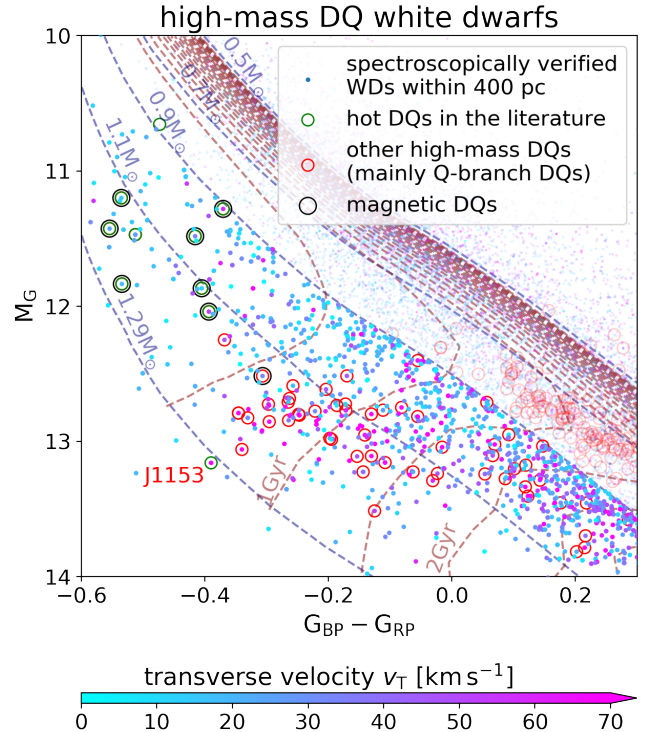


**Figure 8.** A part of the H–R diagram showing the spectroscopically-verified WDs, with Q-branch DQ and hot DQ white dwarfs marked by red and green open circles. We also mark magnetic DQs with larger black circles. Note that the mass range here ( $> 0.9 M_{\odot}$ ) is larger than the sample in our main analysis ( $1.08 - 1.23 M_{\odot}$ ).

Williams et al. 2016), and rarity (e.g., Dufour et al. 2008). On the contrary, we observe that the Q-branch DQ white dwarfs concentrate on the Q branch due to the extra cooling delay, they have helium-dominant atmospheres with about 1% of carbon (Kepler et al. 2015, 2016), and they have undetectable or no magnetic field (see Figure 8). Dunlap & Clemens (2015) discussed one strange ‘hot-DQ’ (SDSS J115305.47 + 005645.8 or J1153) with very high proper motion and therefore thick-disc kinematics. We notice that J1153 has no magnetic field or variability and happens to be on the Q branch (Figure 8), i.e., J1153 is more likely to be a high-mass hot Q-branch DQ rather than a typical hot DQ. Thus, Q-branch DQs and hot DQs have many different apparent characteristics.

We now turn to the similarities between Q-branch DQs and hot-DQs. Firstly, both of them have high masses. Secondly, for both types there are hints of double-WD mergers. For the Q-branch DQs, we have discussed the hint in section 6.1, and for the hot-DQs, Dunlap & Clemens (2015) used proper motion distribution of 12 hot-DQs to argue that they may be mergers products (though, again, based on small number

<sup>4</sup> <http://www.montrealwhitedwarfdatabase.org>

statistics). These two similarities raise the question seriously: *can both hot DQs and Q-branch DQs originate from double-WD mergers and have evolutionary relations?* Here, we use their number counts to explore this possibility. Hot DQs are rare and located in the ‘early’ segment. This is qualitatively consistent with the picture that they are the counterparts of the extra-delayed population diluted in the ‘early’ segment. Quantitatively, the fraction of hot DQs in the region  $\tau_{\text{phot}} < 0.5 \text{ Gyr}$ ,  $m_{\text{WD}} > 0.9 M_{\odot}$  is  $8/198 = 4.0 \pm 1.4 \%$ , based on a spectroscopically-verified white dwarfs sample within 400 pc (as shown in Figure 8). If hot DQs indeed evolve into the Q-branch DQs and the ratio of DQ vs. non-DQ does not change along their evolution, this fraction of hot DQs can be translated into the fraction of extra-delayed population as  $4.0 \% / F_{\text{DQ}} = 4.0 \% / 52 \% = (8 \pm 3) \%$ , in line with the  $f_{\text{extra}} = 7_{-2}^{+2} \%$  obtained from our model.

To summarise, the ‘Q-branch DQs’ should all belong to the extra-delayed population, and they account for  $52 \pm 16 \%$  of this population. We find that they are apparently different from both ordinary standard-mass DQs and hot-DQs. Nevertheless, number counts show that hot DQs may evolve into Q-branch DQs, and there are hints that they both originate from double-WD mergers.

#### 6.4. Double-white-dwarf merger rate

The double-white-dwarf merger is considered to be a promising scenario of Type Ia supernova (i.e., the double-degenerate scenario). In the classical version of this scenario, binary C/O white dwarfs merge by the shrink of orbit due to gravitational wave emission and explode if the total mass of two white dwarfs exceeds the Chandrasekhar limit (Webbink 1984; Iben & Tutukov 1984). The double-WD merger rate is a critical value in this scenario. Simulations of binary population synthesis (BPS) show that the super-Chandrasekhar double-WD merger rate is a few times lower (e.g., Ruiter et al. 2009; Toonen et al. 2012, 2014, 2018) than the observed Type Ia supernova rate, which is  $1.1 \times 10^{-13} M_{\odot}^{-1} \text{ yr}^{-1}$  in a Milky-Way-like galaxy (Li et al. 2011), or a time-integrated rate of  $1.3 \times 10^{-3} M_{\odot}^{-1}$  (Maoz & Graur 2017). However, it is difficult to observationally verify the double-WD merger rate. Existing estimates of the merger rate (including both super- and sub-Chandrasekhar mergers) are made by observing the yet-to-merge binary-WD systems and extrapolating their orbit distribution obtained from multi-epoch radial velocity measurements (Maoz et al. 2012; Badenes & Maoz 2012; Maoz & Hallakoun 2017; Maoz et al. 2018), with its most updated estimate of the merger rate being

$(6.3 \pm 1.0) \times 10^{-13} M_{\odot}^{-1} \text{ yr}^{-1}$  (Maoz et al. 2018), about twice as high as the corresponding value from BPS.

We can use our results from section 5 to estimate the double-WD merger rate in a mass range. To do so, we combine the white dwarf number density and the fraction of merger population. Compared with the method used by Maoz et al. (2018), such an approach is more direct and relies on fewer assumptions, though it probes only a range of final mass:  $1.10 - 1.28 M_{\odot}$  (assuming C/O-cores in white dwarfs; we adopt this mass estimate because the products of double-WD mergers should have C/O cores instead of O/Ne cores). We use white dwarfs in the ‘early’ segment. This region is brighter than 13 magnitude in  $M_G$ , corresponding to  $G < 20$  within 250 pc (the *Gaia* DR2 completeness drops at  $G \sim 20.5$ ), so this sample should be nearly complete. It contains 304 white dwarfs. Using the fraction of merger fraction  $20 \pm 6 \%$  from equation 31, we estimate that the production rate of double-WD mergers with final mass in  $1.10 - 1.28 M_{\odot}$  (assuming C/O-cores in white dwarfs) is

$$304 \times 20 \% / 0.7 \text{ Gyr} = (87 \pm 26) \text{ Gyr}^{-1}, \quad (35)$$

where 0.7 Gyr is the average time-span of the ‘early’ segment. We then estimate the total stellar mass within 250 pc to be  $4.1 \times 10^6 M_{\odot}$ , using the local stellar mass density  $\rho_{\star} = 0.083 M_{\odot} \text{ pc}^{-3}$  (McMillan 2011) and a scale-height of 300 pc. Combining the two values and the simulation result that double-WD mergers lose negligible mass (e.g., Dan et al. 2014), we estimate the recent double-WD merger rate in the Milky-Way disc with  $m_{\text{WD1}} + m_{\text{WD2}}$  ranging  $1.10 - 1.28 M_{\odot}$  (assuming C/O-cores in white dwarfs) to be

$$(2.1 \pm 0.6) \times 10^{-14} M_{\odot}^{-1} \text{ yr}^{-1}. \quad (36)$$

As explained in section 5, this estimate of merger rate does not rely on whether or not the extra-delayed white dwarfs are mergers. If we assume setup 1 and use the number count in the ‘Q branch’ segment to estimate the merger rate, we will get a remarkably similar result,  $(2.3 \pm 0.6) \times 10^{-14} M_{\odot}^{-1} \text{ yr}^{-1}$ , again supporting the idea that the extra-delayed population might be merger products. For comparison, BPS provides a rate of about  $1.6 \times 10^{-14} M_{\odot}^{-1} \text{ yr}^{-1}$  for the same mass range, averaged over Hubble time after a single star-formation event. Since the Milky-Way had a higher star-formation rate at the early time, the current merger rate from BPS should be even lower. In addition, based on BPS results, the super-Chandrasekhar merger rate is about 1–2 times of that in our mass range (Toonen et al. 2014, and private communication). So, our measurement also provides observational evidence that double-WD mergers can contribute to a substantial amount of Type Ia supernovae.

## 7. CONCLUSION

The white dwarf H–R diagram derived from *Gaia* data has revealed a number-density enhancement of high-mass white dwarfs, called the Q branch. This feature is located at the high-mass end of the white dwarf crystallization branch. However, the enhancement is higher than expected for crystallization, suggesting an extra cooling delay. Adding transverse-velocity information to the H–R diagram, we find a clear velocity excess on the Q branch (Figure 1), which indicates that the extra cooling delay is long and influences only a small fraction of high-mass white dwarfs.

Motivated by this simple observation, we then build a model to quantitatively analyze evolutionary delays with respect to the ‘single-star evolution plus standard cooling’. Our model includes two kinds of delay: the extra cooling delay on the Q branch and the double-WD merger delay. According to the age–velocity–dispersion relation (AVR) of milky-way disc stars, velocities can be used as indicators of the true ages of white dwarfs. So, we statistically compare these dynamical ages with their photometric ages to extract information of the two delays. With more than one thousand high-mass white dwarfs ( $1.08 - 1.23 M_{\odot}$ ,  $d < 250$  pc) selected from *Gaia* DR2, our model allows us to constrain the fraction of the extra-delayed white dwarf population, the extra-delay length, and the fraction of double-WD merger products. To eliminate selection effects, we use the conditional probability distribution of velocities given the photometric and positional information of each white dwarf. To avoid systematic errors of the model, we also fit the AVR and solar motion simultaneously with the above three parameters. Having checked that the AVR and solar motion parameters are all in agreement with standard values from the literature and that our best-fitting model provides a good fit to observations, we find that:

1. about 7% of high-mass white dwarfs experience an extra cooling delay of 8 Gyr long when they evolve onto the Q branch;
2. the double-WD merger fraction is  $20 \pm 6\%$  in the mass range  $1.10 - 1.28 M_{\odot}$  (assuming C/O-cores in white dwarfs), corresponding to a double-WD merger rate of  $(2.1 \pm 0.6) \times 10^{-14} M_{\odot}^{-1} \text{yr}^{-1}$ .

This long extra cooling delay is a challenge to white dwarf cooling models. We propose that it may be caused by the energy release of  $^{22}\text{Ne}$  settling, which can explain both its relation to crystallization and the small fraction of the extra-delayed population. The  $^{22}\text{Ne}$  settling favors C- (or C/O-) core white dwarfs, suggesting that the extra-delayed population is likely to originate

from double-WD mergers. This suggestion is further supported by the lack of wide-separation binaries on the Q branch. Since existing models do not explore the same mass range where the Q branch is located, a cooling model including  $^{22}\text{Ne}$  settling for  $m_{\text{WD}} > 1.1 M_{\odot}$  C/O white dwarfs with metal-rich progenitors will be needed to test our explanation. Whether or not  $^{22}\text{Ne}$  settling plays a significant role, investigating this delay is important for further understanding white dwarf physics.

Our velocity analysis also provides a direct observational constraint on the double-WD merger rate. Interestingly, this is independent of the nature of the extra delay or even the explanation of the Q branch. The value we obtained is slightly higher than the prediction from binary population syntheses for the same mass range. Our result also helps to constrain the contribution of double-WD mergers to Type Ia supernova.

## ACKNOWLEDGMENTS

We thank Pierre Bergeron for providing the *Gaia* pass-band photometry of WD models, María E. Camisassa for providing the cooling sequences of O/Ne WDs before they became public, Silvia Toonen for providing the updated results of binary population synthesis in specific mass ranges and comments on our draft, Kareem El-Badry for providing an extended version of the *Gaia* wide-separation binary catalog, and Hsiang-Chih Hwang for pointing out a typo in our code. We thank Pier-Emmanuel Tremblay for his detailed comments and criticisms; his valuable helps improved our draft a lot. We thank J. J. Hermes for his detailed comments and suggestions on our draft, which improved its quality. We also thank Kareem El-Badry, J. J. Hermes, Chao Liu, Kevin Schlaufman, Silvia Toonen, Pier-Emmanuel Tremblay, and Rosemary Wyse for discussions. SC thanks Siyu Yao for her constant encouragement and inspiration. JC would like to acknowledge his support from the National Science Foundation (NSF) through grant AST-1614933. BM thanks the David and Lucile Packard Foundation.

This project was developed in part at the 2019 Santa Barbara *Gaia* Sprint, hosted by the Kavli Institute for Theoretical Physics at the University of California, Santa Barbara.

This work has made use of data from the European Space Agency (ESA) mission *Gaia* (<https://www.cosmos.esa.int/gaia>), processed by the *Gaia* Data Processing and Analysis Consortium (DPAC, <https://www.cosmos.esa.int/web/gaia/dpac/consortium>). Funding for the DPAC has been provided by national institutions, in particular the institutions participating in the *Gaia* Multilateral Agreement.



## APPENDIX

## A. THE 2-D GAUSSIAN TRANSVERSE VELOCITY DISTRIBUTION

The 3-D Gaussian velocity distribution is shown in equation 25:

$$p(\mathbf{v})(\tau) = \frac{\exp[-\frac{1}{2}(\mathbf{v} - \mathbf{v}_0)^T \boldsymbol{\Sigma}(\tau)^{-1}(\mathbf{v} - \mathbf{v}_0)]}{\sqrt{8\pi^3 |\boldsymbol{\Sigma}(\tau)|}},$$

where  $\mathbf{v} = (U, V, W)^T$  and  $\boldsymbol{\Sigma} = \text{diag}[\sigma_U^2(\tau), \sigma_V^2(\tau), \sigma_W^2(\tau)]$  in X, Y, Z coordinates. The PDF of the observed transverse velocity is a rotated and marginalised distribution of this 3-D Gaussian, which is a 2-D Gaussian distribution. The only task then is to find the covariance matrix and mean vector of the 2-D Gaussian. Let  $\mathbf{v}_{XYZ} = (U, V, W)$  and  $\mathbf{v}_{LBR} = (v_L, v_B, v_R)$  be the expressions of the same vector  $\mathbf{v}$  in the two coordinates and matrix  $M$  the rotation matrix from LBR to XYZ coordinate systems:

$$(\mathbf{v} - \mathbf{v}_0)_{XYZ} = M \cdot (\mathbf{v} - \mathbf{v}_0)_{LBR}, \quad (\text{A1})$$

where

$$M = \begin{bmatrix} \sin l & -\sin b \cos l & \cos b \cos l \\ \cos l & -\sin b \sin l & \cos b \sin l \\ 0 & \cos b & \sin b \end{bmatrix}. \quad (\text{A2})$$

Using this expression of  $M$  means that we ignore the small in-disc rotation between the Cartesian coordinate  $XYZ$  and the galactic polar coordinate. Then, we write the 3-D Gaussian distribution in both coordinate systems (note that the Jacobian determinant of rotation transform is unity) and derive:

$$(\mathbf{v} - \mathbf{v}_0)_{XYZ}^T \boldsymbol{\Sigma}_{XYZ}^{-1} (\mathbf{v} - \mathbf{v}_0)_{XYZ} = (\mathbf{v} - \mathbf{v}_0)_{LBR}^T \boldsymbol{\Sigma}_{LBR}^{-1} (\mathbf{v} - \mathbf{v}_0)_{LBR}. \quad (\text{A3})$$

Substituting equation A1, we get:

$$\boldsymbol{\Sigma}_{LBR} = (M^T \boldsymbol{\Sigma}_{XYZ}^{-1} M)^{-1} = M^T \boldsymbol{\Sigma}_{XYZ} M, \quad (\text{A4})$$

where

$$\boldsymbol{\Sigma}_{XYZ} = \begin{bmatrix} \sigma_U^2 & 0 & 0 \\ 0 & \sigma_V^2 & 0 \\ 0 & 0 & \sigma_W^2 \end{bmatrix}. \quad (\text{A5})$$

The covariance matrix  $\boldsymbol{\Sigma}_{LB}$  for the 2-D Gaussian distribution marginalised along the R direction is the first  $2 \times 2$  sub-matrix of  $\boldsymbol{\Sigma}_{LBR}$ . Then, the conditional PDF of the two transverse components  $(v_L, v_B)$  of  $\mathbf{v}$  can be written as:

$$p(v_L, v_B | l, b, \tau) = \frac{\exp[-\frac{1}{2}(\mathbf{v} - \mathbf{v}_0)_{LB}^T \boldsymbol{\Sigma}_{LB}(\tau)^{-1}(\mathbf{v} - \mathbf{v}_0)_{LB}]}{\sqrt{4\pi^2 |\boldsymbol{\Sigma}_{LB}(\tau)|}} \quad (\text{A6})$$

## B. MCMC SETTINGS

In our Bayesian model, we assume uniform distributions for parameter priors. We feed an affine invariant MCMC sampler `emcee` (Foreman-Mackey et al. 2013) with the natural logarithm of likelihood function defined in equation 19. We use 50 walkers to explore the parameter space and start with a first guess of the parameters. After 200 steps of burn-in, the chains are checked to be converged by comparing the percentile values of the parameters in each chain. Then, we run another 400 steps and using this sampling to represent the posterior distribution of each parameter. Figure 9 shows the marginal posteriors of  $f_m$  and the 10 parameters of AVR and their correlations, under the first setup of Table 1, i.e., assuming the extra-delayed population also has merger delay. The second setup has similar results of the AVR.

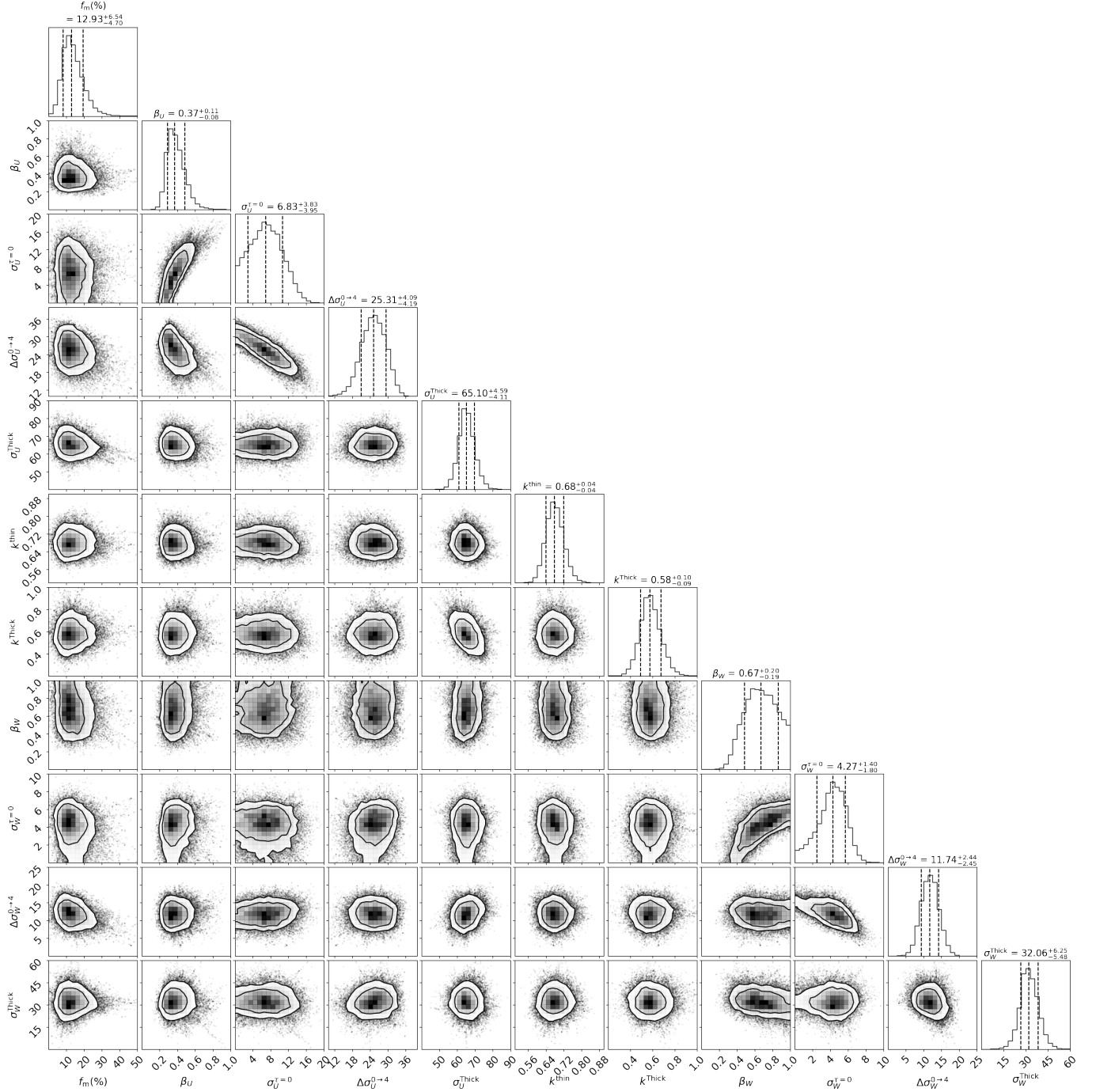


**Figure 9.** The posteriors of all parameters used in our WD model, in which the observables include angular positions of WDs  $l$  and  $b$ , distances  $d$  derived from parallaxes, two components of transverse velocity  $v_L$  and  $v_B$  derived from proper motions and parallaxes, mass  $m_{\text{WD}}$  and cooling age  $t_c$  derived from the H-R diagram and WD cooling model.

### C. THE ENERGY RELEASE OF $^{22}\text{Ne}$ SETTLING

According to Bildsten & Hall (2001), the energy release of  $^{22}\text{Ne}$  settling is nearly constant before crystallization:

$$\begin{aligned}
 L_{\text{Ne}} &\propto FV_{\text{drift}}n(^{22}\text{Ne}) \\
 &\propto f(m_{\text{WD}})\frac{D}{D_s}X(^{22}\text{Ne})Z^{-1.56}T_c^{1/3},
 \end{aligned}
 \tag{C7}$$

where  $F = 2m_p g$  is the net force felt by each  $^{22}\text{Ne}$  nucleus,  $V_{\text{drift}}$  is the drift velocity of the settling,  $n$  is the element number density,  $f(m_{\text{WD}})$  is an increasing function of mass,  $D$  is the diffusion coefficient of  $^{22}\text{Ne}$ ,  $D_s$  is the one-component self-diffusion coefficient (which can be used as a reference value),  $X$  is the element abundance,  $Z$  is the atomic number of the main element in the white dwarf core,  $T_c$  is the core temperature, which scales with the surface temperature  $T_{\text{eff}}$ . So, the white dwarf mass, diffusion coefficient, progenitor metallicity, and core composition will determine the power of energy release from  $^{22}\text{Ne}$  settling.

## REFERENCES

- Althaus, L. G., García-Berro, E., Renedo, I., et al. 2010, *ApJ*, **719**, 612
- Anguiano, B., Rebassa-Mansergas, A., García-Berro, E., et al. 2017, *MNRAS*, **469**, 2102
- Astropy Collaboration, Robitaille, T. P., Tollerud, E. J., et al. 2013, *A&A*, **558**, A33
- Astropy Collaboration, Price-Whelan, A. M., Sipócz, B. M., et al. 2018, *AJ*, **156**, 123
- Badenes, C., & Maoz, D. 2012, *ApJL*, **749**, L11
- Bergeron, P., Dufour, P., Fontaine, G., et al. 2019, *ApJ*, **876**, 67
- Bergeron, P., Wesemael, F., Dufour, P., et al. 2011, *ApJ*, **737**, 28
- Bildsten, L., & Hall, D. M. 2001, *ApJL*, **549**, L219
- Binney, J., & Tremaine, S. 2008, *Galactic Dynamics: Second Edition* (Princeton University Press)
- Bovy, J. 2017, *MNRAS*, **468**, L63
- Camisassa, M. E., Althaus, L. G., Córscico, A. H., et al. 2016, *ApJ*, **823**, 158
- . 2019, *A&A*, **625**, A87
- Cummings, J. D., Kalirai, J. S., Tremblay, P.-E., Ramirez-Ruiz, E., & Choi, J. 2018, *ApJ*, **866**, 21
- Dan, M., Rosswog, S., Brügggen, M., & Podsiadlowski, P. 2014, *MNRAS*, **438**, 14
- Deloye, C. J., & Bildsten, L. 2002, *ApJ*, **580**, 1077
- Dufour, P., Béland, S., Fontaine, G., Chayer, P., & Bergeron, P. 2011, *ApJL*, **733**, L19
- Dufour, P., Bergeron, P., & Fontaine, G. 2005, *ApJ*, **627**, 404
- Dufour, P., Blouin, S., Coutu, S., et al. 2017, in *Astronomical Society of the Pacific Conference Series*, Vol. **509**, 20th European White Dwarf Workshop, ed. P.-E. Tremblay, B. Gänsicke, & T. Marsh, 3
- Dufour, P., Fontaine, G., Bergeron, P., et al. 2010, in *American Institute of Physics Conference Series*, Vol. **1273**, American Institute of Physics Conference Series, ed. K. Werner & T. Rauch, 64
- Dufour, P., Fontaine, G., Liebert, J., Schmidt, G. D., & Behara, N. 2008, *ApJ*, **683**, 978
- Dufour, P., Green, E. M., Fontaine, G., et al. 2009, *ApJ*, **703**, 240
- Dufour, P., Liebert, J., Fontaine, G., & Behara, N. 2007, *Nature*, **450**, 522
- Dufour, P., Vornanen, T., Bergeron, P., & Fontaine, A., B. 2013, in *Astronomical Society of the Pacific Conference Series*, Vol. **469**, 18th European White Dwarf Workshop., 167
- Dunlap, B. H., Barlow, B. N., & Clemens, J. C. 2010, *ApJL*, **720**, L159
- Dunlap, B. H., & Clemens, J. C. 2015, in *Astronomical Society of the Pacific Conference Series*, Vol. **493**, 19th European Workshop on White Dwarfs, ed. P. Dufour, P. Bergeron, & G. Fontaine, 547
- El-Badry, K., & Rix, H.-W. 2018, *MNRAS*, **480**, 4884
- . 2019, *MNRAS*, **482**, L139
- Fontaine, G., Brassard, P., & Bergeron, P. 2001, *PASP*, **113**, 409
- Foreman-Mackey, D., Hogg, D. W., Lang, D., & Goodman, J. 2013, *PASP*, **125**, 306
- Gaia Collaboration, Prusti, T., de Bruijne, J. H. J., et al. 2016, *A&A*, **595**, A1
- Gaia Collaboration, Babusiaux, C., van Leeuwen, F., et al. 2018a, *A&A*, **616**, A10
- Gaia Collaboration, Brown, A. G. A., Vallenari, A., et al. 2018b, *A&A*, **616**, A1
- García-Berro, E., Althaus, L. G., Córscico, A. H., & Isern, J. 2008, *ApJ*, **677**, 473
- García-Berro, E., Hernanz, M., Mochkovitch, R., & Isern, J. 1988, *A&A*, **193**, 141
- Gentile Fusillo, N. P., Tremblay, P.-E., Gänsicke, B. T., et al. 2019, *MNRAS*, **482**, 4570
- Giammichele, N., Bergeron, P., & Dufour, P. 2012, *ApJS*, **199**, 29
- Holberg, J. B., & Bergeron, P. 2006, *AJ*, **132**, 1221
- Holmberg, J., Nordström, B., & Andersen, J. 2009, *A&A*, **501**, 941
- Iben, Jr., I., & Tutukov, A. V. 1984, *ApJS*, **54**, 335
- Isern, J., Hernanz, M., Mochkovitch, R., & García-Berro, E. 1991, *A&A*, **241**, L29
- Isern, J., Mochkovitch, R., García-Berro, E., & Hernanz, M. 1997, *ApJ*, **485**, 308

- Kepler, S. O., Pelisoli, I., Koester, D., et al. 2015, *MNRAS*, **446**, 4078
- . 2016, *MNRAS*, **455**, 3413
- Kowalski, P. M., & Saumon, D. 2006, *ApJL*, **651**, L137
- Lauffer, G. R., Romero, A. D., & Kepler, S. O. 2018, *MNRAS*, **480**, 1547
- Li, W., Chornock, R., Leaman, J., et al. 2011, *MNRAS*, **412**, 1473
- Liu, D., Wang, B., & Han, Z. 2018, *MNRAS*, **473**, 5352
- Mackereth, J. T., Bovy, J., Leung, H. W., et al. 2019, arXiv e-prints. <https://arxiv.org/abs/1901.04502>
- Maoz, D., Badenes, C., & Bickerton, S. J. 2012, *ApJ*, **751**, 143
- Maoz, D., & Graur, O. 2017, *ApJ*, **848**, 25
- Maoz, D., & Hallakoun, N. 2017, *MNRAS*, **467**, 1414
- Maoz, D., Hallakoun, N., & Badenes, C. 2018, *MNRAS*, **476**, 2584
- Maoz, D., Mannucci, F., & Nelemans, G. 2014, *ARA&A*, **52**, 107
- Maoz, D., Sharon, K., & Gal-Yam, A. 2010, *ApJ*, **722**, 1879
- McMillan, P. J. 2011, *MNRAS*, **414**, 2446
- Mennekens, N., Vanbeveren, D., De Greve, J. P., & De Donder, E. 2010, *A&A*, **515**, A89
- Rebassa-Mansergas, A., Rybicka, M., Liu, X.-W., Han, Z., & García-Berro, E. 2015, *MNRAS*, **452**, 1637
- Rowell, N., & Kilic, M. 2019, *MNRAS*, **484**, 3544
- Ruiter, A. J., Belczynski, K., & Fryer, C. 2009, *ApJ*, **699**, 2026
- Sato, Y., Nakasato, N., Tanikawa, A., et al. 2015, *ApJ*, **807**, 105
- Schönrich, R., Binney, J., & Dehnen, W. 2010, *MNRAS*, **403**, 1829
- Segretain, L., Chabrier, G., Hernanz, M., et al. 1994, *ApJ*, **434**, 641
- Sharma, S., Bland-Hawthorn, J., Binney, J., et al. 2014, *ApJ*, **793**, 51
- Shen, K. J., Kasen, D., Miles, B. J., & Townsley, D. M. 2018a, *ApJ*, **854**, 52
- Shen, K. J., Boubert, D., Gänsicke, B. T., et al. 2018b, *ApJ*, **865**, 15
- Siess, L. 2007, *A&A*, **476**, 893
- Toonen, S., Claeys, J. S. W., Mennekens, N., & Ruiter, A. J. 2014, *A&A*, **562**, A14
- Toonen, S., Nelemans, G., & Portegies Zwart, S. 2012, *A&A*, **546**, A70
- Toonen, S., Perets, H. B., Igoshev, A. P., Michaely, E., & Zenati, Y. 2018, *A&A*, **619**, A53
- Tremblay, P.-E., Bergeron, P., & Gianninas, A. 2011, *ApJ*, **730**, 128
- Tremblay, P.-E., Cummings, J., Kalirai, J. S., et al. 2016, *MNRAS*, **461**, 2100
- Tremblay, P.-E., Fontaine, G., Fusillo, N. P. G., et al. 2019, *Nature*, **565**, 202
- Tutukov, A. V., Yungelson, L. R., & Iben, Jr., I. 1992, *ApJ*, **386**, 197
- van Horn, H. M. 1968, *ApJ*, **151**, 227
- Webbink, R. F. 1984, *ApJ*, **277**, 355
- Wegg, C., & Phinney, E. S. 2012, *MNRAS*, **426**, 427
- Williams, K. A., Montgomery, M. H., Winget, D. E., Falcon, R. E., & Bierwagen, M. 2016, *ApJ*, **817**, 27
- Williams, K. A., Winget, D. E., Montgomery, M. H., et al. 2013, *ApJ*, **769**, 123
- Yu, J., & Liu, C. 2018, *MNRAS*, **475**, 1093
- Yungelson, L. R., & Kuranov, A. G. 2017, *MNRAS*, **464**, 1607